*International Journal of Research in Engineering and Science (IJRES)*
*ISSN (Online): 2320-9364, ISSN (Print): 2320-9356*
*www.ijres.org Volume 14 Issue 1 ǁ January 2026 ǁ PP. 173-195*

# Dynamics and Hysteresis of Unfrozen Water Content in Soils During Freeze–Thaw Cycles: A Review

Muhammad Shahab Khan[1]*, Xusheng Wan[1], Ishfaq Ahmad Khan[1], Jishuai Zhu[1]
[*1]*Department of Civil Engineering, Southwest Petroleum University, Chengdu 610500, China*

***Abstract***
*The nonlinear dynamics governing unfrozen water content within soils undergoing freeze–thaw (F–T) cycles profoundly affect ecosystem stability, hydrological processes, and the structural integrity of infrastructure in cold regions. However, current understanding remains limited by inadequate characterization of hysteresis phenomena, primarily due to oversimplified assumptions regarding pore-scale interactions, soil mineralogy, and thermodynamic factors controlling water retention during freezing and thawing. This review systematically synthesizes experimental observations, theoretical insights, and modelling advancements to elucidate the underlying mechanisms responsible for freeze–thaw hysteresis in diverse soil systems. Critical analysis of recent studies highlights significant discrepancies between classical predictive frameworks particularly those based on the Clausius–Clapeyron equation and experimentally observed behaviours, especially in fine-grained soils rich in clay minerals. Advanced experimental techniques, such as low-field nuclear magnetic resonance (NMR), have demonstrated superior efficacy in quantifying unfrozen water content by distinguishing bound from capillary-held water at subzero temperatures, providing clarity on soil-specific freezing behaviours. Furthermore, this review emphasizes the urgent necessity for integrated thermo-hydro-mechanical-chemical (THMC) modelling frameworks, rigorously calibrated against high-resolution field and laboratory datasets. Such interdisciplinary efforts are critical to effectively address climate-driven alterations in permafrost regions and enhance predictive capability for infrastructure resilience and environmental management under accelerating climate warming scenarios.*

***Keywords:*** *Unfrozen water content, Freeze–thaw hysteresis, Soil–water interaction, NMR characterization, Cold-region geotechnics.*

---

Date of Submission: 13-01-2026 Date of acceptance: 29-01-2026

---

## I. Introduction

With the accelerating pace of economic growth and societal development, coupled with the abundant natural resources in cold regions, human activities are increasingly expanding into these environments. Frozen soil, or permafrost, plays a critical role in shaping the ecological, hydrological, and infrastructural dynamics of these regions. Its presence and evolution influence not only the stability of engineered structures but also broader issues of environmental sustainability and resource access. A key aspect of frozen soil behavior lies in the persistence of unfrozen water during subzero conditions. Even when the soil–water system undergoes freezing, not all the water transitions into ice [1]. The content of unfrozen water maintains a dynamic equilibrium with temperature and serves as the primary medium for liquid water migration. This unfrozen fraction significantly affects the thermal, hydraulic, and mechanical characteristics of the soil [2], [3]. The redistribution of water and solutes, prompted by the migration and freezing of this liquid phase, alters hydraulic conductivity, induces frost heaving, and modifies the physical and chemical properties of the soil matrix [4], [5].

In cold climates, the freeze–thaw (F–T) cycle initiates pore structure changes in soil due to repeated ice-water phase transitions. These changes critically affect hydrological seepage behavior, contribute to frost heave and thaw settlement, and ultimately cause uneven deformation in overlying structures. The cumulative impact underscores the necessity of thoroughly investigating the fundamental mechanisms behind F–T dynamics for the advancement of cold-region engineering, hydrological modelling, and climate-adaptive design [6]–[8].

This issue becomes even more critical in permafrost zones, such as the Arctic, where warming subsurface temperatures jeopardize the structural integrity of permafrost a layer that underlies nearly a quarter of the Northern Hemisphere's landmass. Many of these permafrost zones lie just a few degrees below 0°C, rendering them exceptionally sensitive to climatic variations. Permafrost degradation has far-reaching consequences, including the release of methane from thawed organic matter and severe disruptions to infrastructure such as pipelines, roads, foundations, and port facilities that are essential for resource extraction and logistical operations [9], [10].

An important parameter in understanding these phenomena is the unfrozen water content, which governs how frozen soils respond to thermal and mechanical stimuli. It influences not only the soil's strength and

deformation characteristics but also its participation in thermal and hydrological cycles [11]–[14]. Due to the lower thermal conductivity of ice compared to unfrozen water, phase transitions further reduce overall thermal conductivity [15]. Moreover, latent heat exchange during phase change establishes complex source–sink relationships within the thermal and hydrological regimes [16], [17]. The frozen layer's low permeability also restricts the movement of surface and groundwater [18], [19].

Understanding hysteresis in unfrozen water content also holds relevance for practical applications such as forecasting snowmelt timing, modelling surface runoff, and predicting permafrost stability all of which are crucial for environmental planning and disaster mitigation in cold regions [20]–[22]. As infrastructure development and ecological conservation increasingly intersect in high-latitude and high-altitude areas, the study of unfrozen water dynamics through thermodynamically and hydraulically informed models like the SFCC and FTCC offers a critical scientific foundation for sustainable development in these vulnerable landscapes.

Although numerous experimental and theoretical studies have addressed the freeze–thaw behavior of soil–water systems, existing literature generally lacks a comprehensive and systematic explanation of the mechanisms underlying hysteresis during freezing and thawing. Most investigations emphasize individual influencing factors or modelling approaches without integrating the dynamic, nonlinear evolution of hysteresis throughout the freeze–thaw cycle. Moreover, quantitative assessments of the degree of hysteresis and its progression remain limited. In response to these gaps, this review focuses on the nonlinear dynamics and hysteresis characteristics of unfrozen water in soils subjected to freeze–thaw cycles. Specifically, it aims to: (1) elucidate the evolutionary law of freeze–thaw hysteresis based on its mechanistic stages; (2) explore the thermodynamically derived positions of freezing and thawing curves in idealized and natural pore structures (spherical, cylindrical, and irregular); and (3) develop a quantitative index to characterize the hysteresis degree, while analysing its variation throughout the freeze–thaw process. Through this approach, the paper provides a structured understanding of hysteresis formation, modelling challenges, and implications for cold-region geotechnics and hydrology.

## II. Theoretical Background

The presence of a continuous unfrozen water film at the ice–soil interface is well established, with studies confirming its mobility, persistence down to –40 °C, and composition as ordinary hexagonal ice I [23]–[25]. This interfacial water behaves like a two-dimensional liquid, enabling molecular and solute movement within the confined zone [26], [27]. Temperature is the primary factor governing unfrozen water content, followed by pressure, which increases unfrozen water at fixed temperatures [28], as well as solute concentration consistent with freezing point depression principles [8, 18], and the effects of soil particle geometry and freezing conditions [29]. These relationships are captured by the Soil Freezing Characteristic Curve (SFCC), which quantifies unfrozen water relative to temperature and underpins simulations of coupled heat and moisture transfer in frozen ground [30]–[33]. SFCCs are often modelled using power exponential functions, attributed either to capillary effects from pore size distributions [32], [34] or to surface forces between adsorbed water films and soil particles [35], [36], with integrated models suggesting both factors contribute depending on pore geometry, soil texture, and freezing conditions [37], [38]. Extending this framework, the Freezing–Thawing Characteristic Curve (FTCC) incorporates the Soil Thawing Characteristic Curve (STCC) to continuously represent temperature, unfrozen water, and matric suction across freeze–thaw cycles [8], [39], [40], thereby improving understanding of moisture migration and permafrost behavior [41], [42] and supporting models of coupled heat–water–mass transport [43]. A consistent feature of the FTCC is hysteresis higher unfrozen water during freezing than thawing at identical temperatures caused by nucleation pathways, ice lensing, and pore-scale dynamics [44], [45]. Accurately representing this behavior is essential for hydrological modelling, geotechnical assessments, and infrastructure resilience in cold regions.

### 2.1 Soil Freeze–Thaw Mechanisms

The process of soil freezing, especially when influenced by supercooling, unfolds in four distinct phases: the supercooling, nucleation, equilibrium, and final freezing stages [46]. Initially, during supercooling, the temperature of the soil drops below its normal freezing point without initiating crystallization, meaning that the pore water remains in a metastable liquid state [47]. When the temperature reaches a critical threshold, a sudden inflection in the thermal curve marks the onset of nucleation. At this juncture, initial ice nuclei begin to form as clusters of water molecules coalesce, triggering further molecular alignment around these centers. This crystallization releases latent heat, temporarily increasing the soil temperature [48]–[50].

Subsequently, in the equilibrium stage, ice crystals grow progressively while the majority of free water rapidly solidifies. A thermal balance is established between external cooling and the internal release of latent heat, stabilizing the temperature near the soil's freezing point. The duration of this phase depends largely on the amount of freezable water remaining in the unfrozen fraction of the soil. As the process continues into the final stage, the

remaining bound water gradually solidifies. Once the majority of phase change is complete, further cooling occurs without additional latent heat release [51], [52].

Importantly, the temperature at which initial crystallization occurs referred to as the supercooling point is distinct from the conventional freezing point. When this critical supercooling temperature is reached, latent heat is released as phase transition begins within the remaining liquid water fraction. Thawing, in contrast, proceeds differently. At subzero temperatures, melting initiates with the ice embedded in finer pores, where minimal temperature variation is observed despite ongoing phase change due to localized energy absorption [53], [54]. As warming progresses, ice in larger pores begins to melt, causing a rapid rise in heat absorption until full phase transition is achieved. In high-temperature permafrost, considerable phase transformations may occur below 0°C. Observational data suggest that the complete melting temperature exhibits a slight positive shift with increasing initial water content, reflecting the additional energy needed to transition from an ice–water mixture into a fully liquid state [55], [56].

Several notable studies have deepened our understanding of unfrozen water behavior during these transitions. Kozlowski, using Differential Scanning Calorimetry (DSC), identified key thermal points such as the supercooling, freezing, and melting temperatures [3], and proposed a semi-empirical model to estimate changes in unfrozen water content, particularly in clay-rich soils [57]. His work offers a framework that blends theoretical rigor with empirical calibration [58]. Similarly, Tsytovich linked unfrozen water behavior to parameters such as the plasticity index and the soil's thermal state [59], while Tice et al., developed an exponential empirical equation grounded in soil particle surface area to quantify non-frozen water in reconstituted clay samples [60].

Akayawa's experimental surveys yielded a broad dataset on soil-dependent variability in model parameters, although heterogeneity in results suggests sensitivity to soil type and structure [61]. In response, Michalowski advanced a three-parameter model to better characterize the non-linear response of unfrozen water in permafrost [62]. These models collectively illustrate that even within a single soil category, microstructural differences can introduce considerable variability in predicted unfrozen water content. A related challenge concerns how unfrozen water content is measured experimentally, which directly affects model calibration and comparison across studies [63], [64]. Current measurement techniques include calorimetry (e.g., differential scanning calorimetry, which infers unfrozen water from phase-change enthalpy), pulse nuclear magnetic resonance (NMR) [44], frequency-domain reflectometry (FDR) [65], finite-difference time-domain (FDTD)–based electromagnetic inversion [66], and time-domain reflectometry (TDR) [67]. However, these experimental techniques are typically implemented only along the freezing path and thus often neglect supercooling and thawing behavior. Moreover, measurement protocols that sample unfrozen water content at relatively coarse, discrete temperature intervals provide insufficient resolution to describe the continuous evolution and hysteresis of freeze–thaw transitions [68], [69].

### 2.2 Influence of Soil Characteristics On Unfrozen Water Content

The unfrozen water content ($\theta_u$) in frozen soils is not only temperature-dependent but also highly sensitive to soil-specific characteristics, which govern water retention and phase transition processes during freezing [70]. Among these, the initial water content is a key determinant, as soils with higher degrees of saturation retain significantly more unfrozen water than those with lower saturation levels (Sr = 0.6–0.7) [71], owing to the greater availability of free pore water that resists complete freezing [72]. Soil composition exerts an equally strong influence: fine-grained soils, particularly those with high clay content, maintain larger quantities of unfrozen water than coarse-textured soils, due to their high surface area and strong adsorption capacity [73]. Furthermore, the mineralogical type of clay is critical, as montmorillonite-rich soils display higher unfrozen water retention compared to kaolinite, reflecting differences in interlayer hydration and electrostatic interactions [38], [74]. Particle size distribution also plays a decisive role, with silts and clays promoting water–ice segregation and capillary retention, whereas sands with larger pores allow for more complete freezing at higher temperatures [75], [76]. Together, these factors highlight the complex interplay between soil texture, mineralogy, and moisture conditions, all of which must be considered for accurate prediction and modeling of $\theta_u$ in frozen soils.

The unfrozen water content ($\theta_u$) in frozen soils is also influenced by a combination of intrinsic and environmental factors, including initial moisture levels, freeze–thaw history, bulk density, and a variety of soil-specific characteristics such as particle size distribution, total clay fraction, and the presence of specific clay minerals [38], [77], [78]. The thermal dependency of $\theta_u$ is typically described using the Soil Freezing Characteristic Curve (SFCC), which expresses the relationship between temperature and unfrozen water. Numerous studies have contributed to defining this curve [7], [79], [80]. In one notable study conducted on silty clay from the Qinghai–Tibet Plateau, Wen et al., (2012) demonstrated that both the initial water content and the amount of clay significantly impacted the freezing temperature and $\theta_u$ [81].

Although $\theta_u$ is clearly sensitive to soil composition at identical thermal states, few investigations have systematically quantified how specific soil properties influence it. Most previous works have focused narrowly on total clay content (Kozlowski & Nartowska, 2013; Kruse & Darrow, 2017; Tian et al., 2018; Zhang et al.,

2020), often overlooking the distinction between total clay and clay mineral content. It is important to note that clay is a fine-grained material composed in part of clay minerals, which are hydrous aluminum phyllosilicates. Since these components affect water retention differently, a deeper understanding of how particle gradation, clay content, and mineral composition collectively influence $\theta_u$ is necessary for advancing predictive modeling and interpretation in cryospheric soil research.

Soil water is commonly categorized based on its binding state into gravitational (bulk), capillary, and bound water. Bound water exists within the electrical double layer surrounding soil particles, while water outside this layer is typically either capillary or gravitational in form. The distribution of these water types varies with soil texture and mineralogy (Chai et al., 2018; Mu et al., 2018). For accurate interpretation of $\theta_u$ and its controlling factors, it is essential to differentiate between these water types within the pore structure. NMR not only facilitates $\theta_u$ quantification but also allows researchers to classify pore water based on its mobility, using $T_2$ relaxation time distributions (Coates et al., 1999; Tian et al., 2018; Yuan et al., 2018). These $T_2$ cutoffs help distinguish bound from free water in soils. Although most research in this area has focused on rocks such as sandstones and shales (Bouton et al., 1996; Morriss et al., 1997; Saidian & Prasad, 2015), soil-specific studies are still limited. For example, Tian et al. (2018) identified a $T_2$ threshold of 5.8 ms to separate capillary from bound water in soils with varied clay contents, but their experiments were constrained to a narrow temperature range (–4 °C to 7.5 °C), limiting the ability to distinguish bulk water. Hence, further application of $T_2$ analysis across wider temperature intervals is essential for refining pore water classification in frozen soils.

In parallel with experimental advances, a number of analytical models have been developed to predict $\theta_u$ as a function of temperature. These include volumetric models based on exponential relationships between saturation and temperature (McKenzie et al., 2007), as well as power-law models (Zhang et al., 2017). Additionally, gravimetric approaches have been proposed to correlate mass-based $\theta_u$ with temperature variation (Anderson & Tice, 1972; Kozlowski, 2007; Michalowski, 1993). Such models are valuable tools for reducing dependence on experimental procedures and supporting large-scale simulations. However, their applicability is often restricted by the specific conditions under which they were derived. Validation under broader soil types and environmental conditions remains necessary to enhance their generalizability.

## III. Measurement of Unfrozen Water Content in Soils

The determination of unfrozen water content in soils under freezing conditions has evolved significantly with advancements in measurement science. A variety of laboratory and field-based techniques have been employed to quantify θu , each underpinned by distinct physical principles and characterized by varying degrees of resolution, invasiveness, and thermal sensitivity. This section examines experimental investigations that characterize unfrozen water content in freezing soils, with a focus on the measurement techniques, thermal controls, and calibration procedures that underpin data reliability.

### 3.1 Electromagnetic Measurement Techniques

#### 3.1.1 Nuclear Magnetic Resonance (NMR)

Nuclear magnetic resonance (NMR) logging is widely applied in petroleum and gas exploration to measure the magnetic moment of hydrogen nuclei within fluid-filled pore spaces of reservoir rocks. Since these protons occur in pore fluids, NMR is highly sensitive to oil, gas, and water, providing information on their volume, viscosity, and distribution [82]. The central measurement is the $T_2$ decay, which is analysed to determine porosity and separate bound from free fluids, with permeability estimated through models such as the Timur-Coates or SDR transforms [83]. Relaxation behavior is mainly controlled by grain-surface interactions, where hydrogen protons transfer spin energy to the solid matrix. Because relaxation rates depend on the surface-to-volume ratio, small pores cause faster relaxation while larger pores relax more slowly, enabling assessment of pore-size distributions and reservoir quality [84].

Low-field nuclear magnetic resonance (NMR) is extensively applied to quantify unfrozen water in freezing soils by measuring the transverse relaxation time ($T_2$), which reflects water mobility and confinement within pore structures [83], [84]. $T_2$ enables differentiation among capillary, film, and residual water, as demonstrated in studies by Chen *et al.,* (2021) [85] and Zou *et al.,* (2023) [86] using CPMG pulse sequences to analyse soil freezing characteristic curves (SFCCs) and multi-phase transitions.

Chen *et al.,* (2021) employed a temperature-controlled NMR setup to resolve the volumetric evolution of unfrozen water, using $T_2$ distributions to partition it into distinct phases and construct phase-specific SFCCs [85]. The relaxation behavior arises from combined effects of free, surface, and diffusive mechanisms, governed by the expression [87], [88]:

$$\frac{1}{T_2} = \frac{1}{T_{2,free}} + \frac{1}{T_{2,surf}} + \frac{1}{T_{2,diff}} \quad (1)$$

In fine-grained soils, surface relaxation dominates due to negligible free relaxation and limited diffusion, rendering $T_2$ an effective proxy for pore size and water binding status. To quantify the unfrozen water content (θ), Chen *et al.,* developed a temperature-dependent calibration model to correct the magnetization signal, which is inherently influenced by thermal conditions. The corrected magnetization $M^0_m$ is expressed as a linear function of temperature *T*:

$$M_m^0 = \alpha - \beta T \tag{2}$$

where α and β are empirical coefficients determined for each soil sample. The volumetric unfrozen water content is then calculated by:

$$\theta(T) = \left(\frac{M_m^0}{M_t^0}\right)(1 - \theta_s) + \theta_s \tag{3}$$

Here, $M^0_t$ denotes the magnetization at full saturation, and $\theta_s$ represents the porosity of the soil. This formulation accounts for both the thermally induced decline in signal strength and the structural characteristics of the tested soil [89], [90].

Soil samples underwent stepwise freezing from +15 °C to −30 °C in 13 intervals, with 30-minute equilibrium periods before NMR measurements using the Carr–Purcell–Meiboom–Gill (CPMG) sequence. $T_2$ distribution curves enabled separation of unfrozen water into bulk ($T_2 > 20$ ms), capillary (5–20 ms), and bound ($T_2 < 5$ ms) water, reflecting degrees of confinement (Fig. 1a). Silty clay samples S1 and S2 (Sejila Mountain Pass) and C (Cuomujiri Ice Lake) were collected from the Yarlung Zangbo River Basin (~4300 m elevation) (Fig. 1b). Extracted 50 mm below the surface, samples were oven-dried, sieved, and analyzed for particle size (Fig. 1c) and mineralogy via XRD using Jade 6 software. For NMR testing, soils were compacted into Teflon molds (25 mm × 60 mm) at 1.5 g/cm³ dry density, yielding porosities of 42.16%, 43.55%, and 34.67% for S1, S2, and C, respectively. Freezing induced exponential decline in θ, with the sharpest transitions between −1.5 °C and −15 °C. Progressive leftward shifts in $T_2$ peaks confirmed the conversion of mobile water to more constrained phases (Fig. 1d–f) [85].

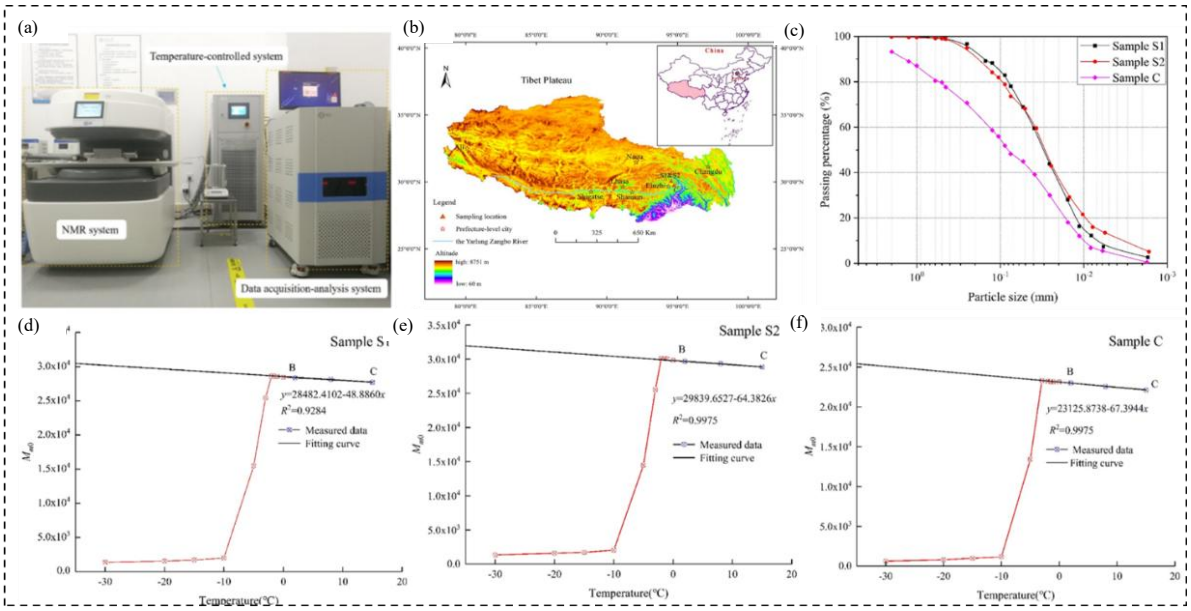


**Figure 1** Schematic layout of the **(a)** temperature-controlled NMR apparatus designed for continuous in-situ thermal monitoring. **(b)** Geographical locations from which soil specimens S1, S2, and C were obtained. **(c)** Comparative analysis of the particle size distribution (PSD) profiles for samples S1, S2, and C. **(d–f)** Calibration curves of unfrozen water content (θu) for soil types S1, S2, and C, derived using temperature-corrected NMR signal intensities [85].

Zou *et al.,* (2023) utilized low-field NMR to quantify unfrozen water content across seven soil types of expansive soil, clay, silt, loess, dispersed soil, red soil, and sandy soil over a temperature range from +20 °C to −80 °C [91]–[93]. The study aimed to develop a predictive model linking unfrozen water content to temperature and soil characteristics under extreme freezing conditions. Leveraging the fact that only hydrogen nuclei in liquid water emit detectable NMR signals, the technique enabled selective measurement of unfrozen water. The system combined cryogenic controls with NMR instrumentation, including a magnet cabinet, controller, and cooling unit. Samples (20 mm × 60 mm, dry density 1.7 g/cm³) underwent staged cooling at 22 temperature points, each held for 1 hour prior to scanning [86].

Watanabe and Osada (2016) conducted thawing experiments on saturated silt loam and sand using an acrylic column with dimensions of 78 mm in diameter and 30 mm in height. Dual temperature-control devices were applied at both ends of the column, subjecting the soil to a freezing temperature of −4.5 °C for 24 hours followed by a 1-hour thawing period at 0 °C [96]. During the thawing phase, upward water flow was maintained at a velocity of 0.53 m/day. Unfrozen water content was quantified using NMR, while thermal conditions were monitored using thermocouples. In an earlier study, Watanabe *et al.,* (2011) explored thawing behavior in unsaturated clayey silt, sand, and clay. Soil specimens were packed into cylindrical cells (17.3 mm diameter, 25 mm height), initially frozen to −20 °C and then progressively warmed to 0 °C in temperature steps, each held for approximately 2 hours until thermal equilibrium was reached. The unfrozen water content was determined using NMR at each interval [97]. Ma *et al.,* (2017) evaluated the thermal response and water retention properties of silt and clay during thawing. Samples were statically compacted into Teflon cylinders with a cross-sectional area of 16 cm² and height of 2 cm and subjected to a controlled warming regime from −40 °C to 20 °C. NMR was employed for measuring the corresponding unfrozen water content [98]. Black and Tice (1989) conducted laboratory experiments on silty sand samples with a total volume of 8 cm³. Freezing and thawing cycles were applied in a constant-temperature bath, maintaining each temperature increment for 45 minutes. NMR techniques were used to track the evolution of unfrozen water [99].

NMR logging offers mineralogy-independent porosity and pore-size distribution, providing more reliable results than conventional logs [100]. It distinguishes bound from free fluids, estimates permeability from $T_2$ distributions, and identifies the type and number of hydrocarbons and water present [101]. However, it is less responsive to low-hydrogen fluids such as gas, requires corrections, and is sensitive to shale content and fluid heterogeneity, which complicate interpretation. In addition, NMR tools have limited depth of investigation, and the technology is costly and technically demanding, requiring specialized expertise for operation and data analysis [102].

**3.1.2 TDR**

Time Domain Reflectometry (TDR) is a non-destructive probing technique that measures the dielectric properties of a medium by transmitting a fast electromagnetic pulse through a waveguide typically a coaxial cable connected to parallel probe rods and observing the reflection time of the pulse [103]. The travel time between the initial and return reflections is used to calculate the apparent dielectric permittivity, $Ka$, of the medium, which is directly related to parameters like moisture content (bulk dielectric constant) [104]. The propagation velocity $v$ in the material is given by:

$$v = c[\varepsilon(\theta)]^{-\frac{1}{2}} = \frac{2L}{\Delta t} \tag{4}$$

where $c$ is the speed of light in a vacuum, $L$ is the probe rod length, $\Delta t$ is the two-way travel time, and $\varepsilon(\theta)$ is the real part of the complex dielectric permittivity dependent on moisture content $\theta$. Materials like water (dielectric ≈ 80) contrast sharply with soil minerals (≈ 3–5) and air (≈ 1), making TDR highly sensitive to water content [105]. The distinctive waveform reflections at probe interfaces allow precise determination of travel time and dielectric measurement.

Zhou *et al.,* (2014) examined sandy silt samples prepared in columns (5.3 cm diameter, 23.6 cm height) across four different saturation levels. Freezing was induced using Peltier elements located at both ends of the column, and water content was measured via TDR [106]. In a separate study, Caicedo (2017) explored freezing dynamics in fine sand and silt samples packed into an acrylic tank measuring 1 × 1 × 0.1 m. Boundary temperatures were fixed at the top and bottom of the tank, and unfrozen water content was assessed using capacitive moisture sensors [107]. Williams (1964) investigated freezing dynamics in silt samples with a total volume of 120 cm³. A steady heat flux was applied via an external cooling vessel to induce freezing from 0 °C down to −3 °C. The associated phase-change water content was measured calorimetrically [94]. Flerchinger *et al.,* (2006) performed field-based monitoring of freezing and thawing cycles in sandy silt. Using TDR probes and thermocouples installed at 5 cm and 10 cm depths, hourly measurements of temperature and unfrozen water content were recorded over a seasonal period. These temporal datasets were digitized for detailed analysis [108].

Azmatch *et al.,* (2012) evaluated the effect of consolidation pressure on freezing behavior in silt. The material was first prepared as a slurry and consolidated under 50 kPa and 100 kPa. Post-consolidation, samples were cooled in a controlled thermal bath and TDR was used to measure the remaining unfrozen water [109]. Spaans and Baker (1996) recorded in-situ freezing data for fine silt at a depth of 29 cm. Unfrozen water content was obtained using TDR instrumentation under natural field conditions [110]. Newman and Wilson (1997) examined freeze–thaw behavior in silt compacted into cylindrical molds (3.81 cm diameter, 10.16 cm height). The samples were subjected to controlled cooling in a temperature-regulated bath, and unfrozen water content was quantified using calorimetry [111]. Liu *et al.,* (2012) conducted freeze–thaw studies on sandy clay and silty clay at the element scale, utilizing TDR to capture unfrozen water content throughout laboratory-imposed thermal

cycles. Samples were initially frozen in a laboratory freezer and subsequently thawed under ambient conditions [112].

Koopmans and Miller (1966) conducted controlled freeze–thaw tests on saturated coarse silt, clayey silt, and fine silt. Specimens measuring 1.2 cm in diameter and up to 10 cm in height were placed in a temperature-controlled bath and cooled from 0 °C to −1.5 °C in increments of approximately 0.05 °C. Each step was held for 24 hours to ensure phase stability. Unfrozen water was measured using a dilatometer [113]. Ren and Vanapalli (2019) studied the freeze–thaw response of silty clay and lean clay samples compacted into 50 mm diameter and 100 mm height cylinders. Freezing progressed from 0 °C to −18 °C, with each temperature level maintained for 12 hours. The unfrozen water content was monitored using a frequency-domain reflectometry (FDR) moisture sensor [64].

A major strength of TDR is its accuracy, non-destructiveness, and independence of soil type, enabling straightforward in situ and profile measurements of volumetric water content. Its rapid response and reliability make it a preferred choice in hydrology, agriculture, and construction [114]. However, TDR has limitations like high bulk electrical conductivity or salinity may attenuate pulse reflections, reducing accuracy though coating probes with epoxy can mitigate but change calibration. Furthermore, accurate interpretation relies on high-quality TDR waveforms and precise determination of reflection times, which depend on both probe design and the dielectric relaxation properties of the material [115].

### 3.2 Observations on Unfrozen Water Variation

#### 3.2.1 Identification of Different Types of Unfrozen Water Using Two $T_2$ Cutoffs

In order to distinguish between bound water and capillary water, Chen *et al.,* used two cutoff values for $T_2$ relaxation time: 0.1ms and 7.4ms. The use of dual cutoff values allowed for a more refined classification of the different types of water present in the soil. The first cutoff, 0.1ms, was used to separate bound water from the rest of the water content. Bound water in this context refers to water molecules that are tightly adsorbed to the surfaces of soil particles and are characterized by extremely short relaxation times due to limited mobility. The second cutoff value, 7.4ms, was introduced to differentiate between bound water and free or capillary water, which exists in larger pores and displays greater mobility.

The $T_2$ distributions indicated that as the temperature decreased, the relaxation time became shorter, and the overall $T_2$ peak shifted leftward. This leftward shift corresponded to a progressive reduction in the proportion of free water and an increase in the relative proportion of bound water. When the temperature reached values below the freezing point, a significant portion of the capillary water transitioned into ice, leaving behind only the more strongly bound water with shorter $T_2$ values. These behaviors were particularly evident in the $T_2$ spectra of the S1, S2, and C soil samples tested at different sub-zero temperatures. Furthermore, the study identified a secondary, minor peak in the long-relaxation-time region at higher temperatures, which gradually disappeared as temperature dropped, signifying the freezing of water in larger pores [52].

#### 3.2.2 Temperature-Induced Changes in Unfrozen Water Content

The relationship between temperature and unfrozen water content was investigated systematically for all three soil samples using the $T_2$ relaxation spectrum measured by NMR [50]. The unfrozen water content ($\theta_u$) decreased significantly with decreasing temperature. At temperatures close to 0 °C, a substantial amount of water remained in an unfrozen state, especially within the capillary pores of coarse soil matrices. However, as temperature dropped, the capillary water froze rapidly, particularly in soils with larger pore diameters. This resulted in a steep decline in the overall unfrozen water content between 0 °C and −4 °C. Below −4 °C, the freezing rate slowed, and the remaining water was primarily in the form of bound water. In this stage, the decline in $\theta_u$ with temperature was much more gradual [52], [85], [116], [117].

Sample S1, characterized by the lowest clay content, exhibited a pronounced decline in unfrozen water content ($\theta_u$) across the freezing range, whereas samples S2 and C, which contained higher clay fractions, showed a more gradual reduction, reflecting their enhanced capacity to retain water in unfrozen form. The $\theta_u$–T curves revealed two distinct freezing regimes: an initial rapid phase associated with capillary water, followed by a relatively stable phase governed by bound water. Among the tested soils, sample C consistently retained the highest $\theta_u$, while S1 maintained the lowest at all temperatures. The critical temperature interval between 0 °C and −4 °C corresponded to the most significant decrease in $\theta_u$, beyond which the decline became less pronounced, underscoring the predominance of bound water and the role of mineral surface interactions in water retention at lower temperatures [85]. These consistent patterns across all samples confirm that finer-textured, clay-rich soils sustain greater unfrozen water content under subzero conditions and highlight the effectiveness of NMR in quantifying dynamic water behaviors in permafrost and cold-region soils.

### 3.2.3 Influence of Clay Content on the Unfrozen Water Content

The study further analyzed how clay content specifically affects the soil's capacity to retain water in an unfrozen state at sub-zero temperatures. By comparing the unfrozen water content of three soil samples S1, S2, and C each with progressively increasing clay fractions, a direct relationship between clay content and $\theta_u$ was established. Sample C, with a clay content of 31.6%, retained the highest amount of unfrozen water throughout the entire temperature range, followed by S2 with 25.1% and S1 with 20.5%. This trend demonstrated that higher clay content significantly enhances a soil's ability to hold water even as temperature decreases [85].

This retention behavior is primarily attributed to the large specific surface area and high adsorption capacity associated with clay minerals. Water molecules tend to form tightly bound hydration layers around these mineral surfaces, and this adsorbed water resists phase change even under freezing conditions [118], [119]. Additionally, clay-rich soils typically contain a higher proportion of micropores, which limit ice nucleation and favor the retention of bound water. The influence of clay on freezing behavior was not only evident in volumetric water content but also in the observed shifts in the NMR relaxation spectra, where clay-rich samples displayed $T_2$ peaks concentrated in shorter relaxation times, indicative of restricted water mobility [120].

Comparative influence of clay content shows $\theta_u$–T relationship for all three samples (Fig. 2). The curve profiles shows that freezing process was delayed and more gradual in the sample with higher clay content. This behavior can be explained by the higher suction potential and water-binding energy associated with fine-grained soil particles. As temperature dropped, the transition from free to bound water became increasingly soil-specific, with more pronounced water retention in finer soils [121].

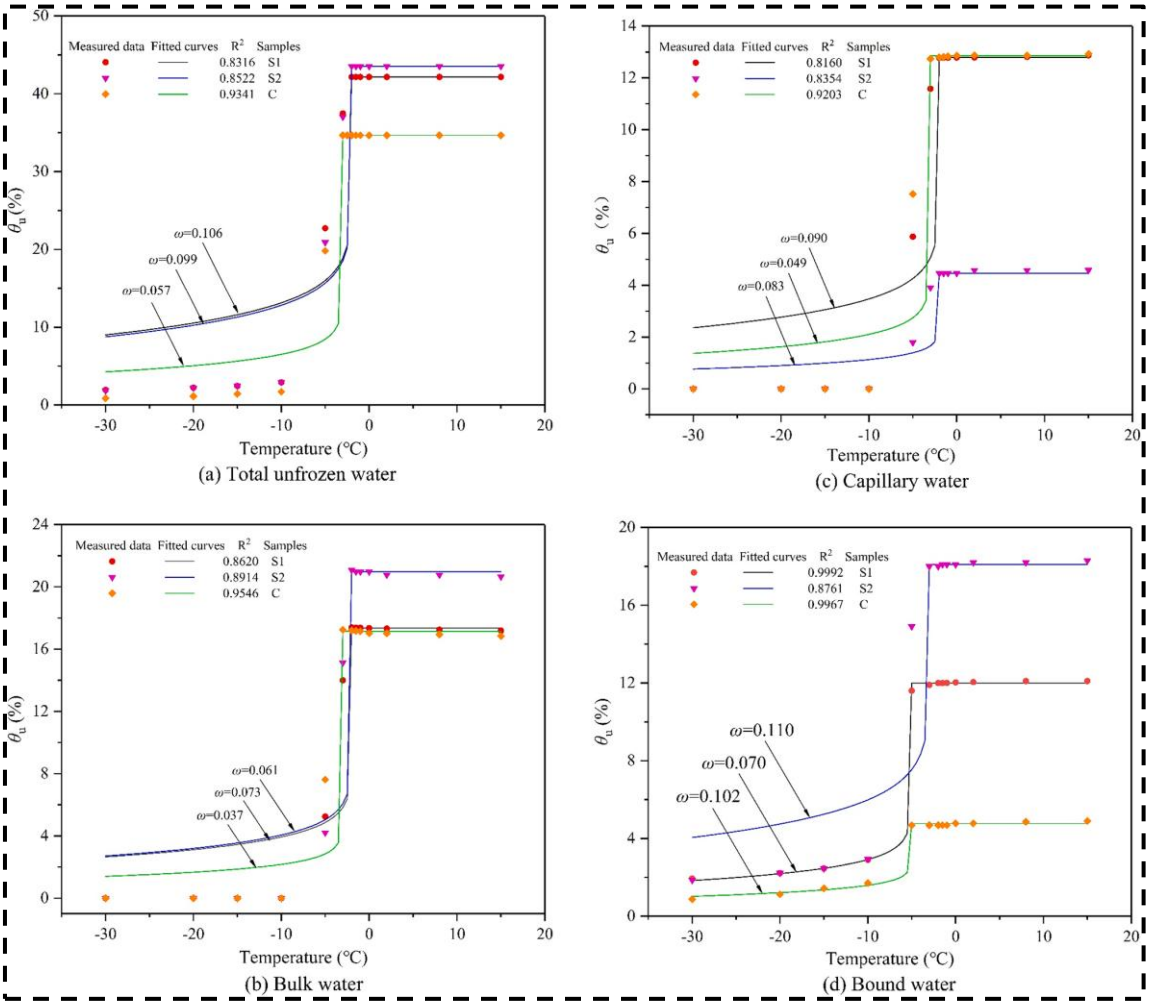


**Figure 2 Comparison of fitted curves using the Zhang et al. (2017) [121] model with NMR-measured data for various water types in soil samples S1, S2, and C.**

## IV. Modelling Frameworks for Soil-Specific Freezing Behavior

Understanding the hydraulic dynamics of frozen soils remains a significant challenge due to the inherent complexity of freeze–thaw mechanisms. As a result, many studies either draw parallels with observations made in unfrozen soils or rely heavily on theoretical formulations to interpret these behaviors. A key factor influencing

water retention in frozen soils is the presence of unfrozen water, whose quantity is closely related to soil surface area and pore morphology. Empirical studies have demonstrated that this relationship often follows power-law trends as temperature decreases [31]. To better capture this behavior, researchers have developed soil freezing curves (SFCs) using conceptual analogues drawn from models originally formulated to represent soil–water retention curves (SWRCs) in unfrozen systems. These SWRC models describe how water content evolves during drying and wetting cycles, where liquid water and gas coexist in the pore spaces [99], [113], [124], [125].

The theoretical basis linking the SWRC and the SFC lies in thermodynamic principles, particularly the Clausius–Clapeyron relationship. This equation relates phase equilibria to pressure and temperature changes and is derived from the Gibbs–Duhem equation, considering the coexistence of two phases typically ice and liquid water within soil pores. It allows for the quantification of suction pressures that develop during freezing, such as unfrozen water suction ($P_{uc} = u_a - u_w$) and cryogenic suction ($P_c = u_l - u_i$), where $u_a$, $u_w$, $u_l$, and $u_i$ represent air pressure, water pressure, liquid pressure, and ice pressure, respectively. The resulting expression, formulated by combining and rearranging these thermodynamic terms, has been refined by Kurylyk and Watanabe (2013) to account for complex phase interactions during freezing transitions [5].

$$\frac{\mathrm{dP}_{\omega \mathrm{f}}}{dT} = \frac{L_{f\rho\omega}}{(\mathrm{T} + 273.15)} \tag{5}$$

The modelling of soil freezing behavior is governed by several fundamental thermodynamic parameters, including pore water pressure ($P_{wf}$, kPa), latent heat of fusion ($L_f$, J/kg), water density (ρw, kg/m³), and temperature (*T*, °C). Building on the analogy between freezing–drying and thawing–wetting processes, the Clausius–Clapeyron (C–C) equation has been widely adopted to convert soil–water retention curves (SWRCs) into soil freezing curves (SFCs), following the classical framework proposed by Koopmans and Miller (1966) [113]. Recognizing the limitations of direct analogies, particularly in fine-grained soils, they introduced a correction factor to account for disparities in surface energy between ice–liquid and air–liquid interfaces. This correction coefficient varies depending on the dominant water retention mechanism ranging from 1.0 under adsorption-dominated conditions to 2.2 when capillarity prevails.

While the C–C formulation offers a valuable theoretical construct, its practical application is constrained by several underlying assumptions. These include the equivalence of ice pressure to atmospheric or overburden pressure, a thermodynamically closed system, and the presumption of quasi-static phase transitions. Such conditions may be reasonable in deeper soil strata but often break down in shallow layers subject to rapid freeze–thaw dynamics. Consequently, this leads to discrepancies between modelled and observed behavior, such as the overestimation of cryosuction-driven migration and premature predictions of ice formation. Similarly, thawing events may produce non-equilibrium pressure responses without commensurate thermal changes. Thermal gradients may also instigate anomalous water redistribution beneath ice lenses, contravening the static assumptions embedded in the model. A critical limitation of the C–C framework is its inability to encapsulate the hydraulic hysteresis introduced by freeze–thaw cycling. Such hysteresis fundamentally alters water and gas transport pathways in frozen soils, influenced by supercooling phenomena, solute concentration effects, and irreversible microstructural transformations. These complexities underscore the inadequacy of employing a single equilibrium-based model to describe dynamic hydrological responses in seasonally frozen or permafrost-affected landscapes. To address these limitations, researchers have adapted soil–water retention models into SWCC-based models using thermodynamic principles to develop practical formulations that estimate unfrozen water content under freezing conditions**.**

### 4.1 Soil Freezing Characteristic Curve Models

#### 4.1.1 van Genuchten Models

The van Genuchten-Bittelli model [126] extends the classical van Genuchten soil water characteristic curve (SWCC) into freezing conditions by incorporating Clapeyron equation-based thermodynamic equilibrium. They assumed pore water pressure as equivalent to negative matric potential, and disregarded soil overburden pressures. Hence, unfrozen water content directly relates to latent heat, gravitational constant, and fitting parameters originating from the SWCC model. Here, $\theta_u$ is the unfrozen water content, $\theta_s$ and $\theta_r$ are the saturated and residual water contents, respectively. $L_f$ is the latent heat of fusion, T is temperature (°C), g is gravitational acceleration, and $T_0$ is reference temperature. $a_v$, $n_v$, and $m_v$ are van Genuchten fitting parameters. :

$$\theta_u = (\theta_s - \theta_r)\left[1 + \left(-\frac{a_v L_f T}{g T_0}\right)^{n_v}\right]^{-m_v} + \theta_r \tag{6}$$

The van Genuchten-Nishimura approach integrates a simplified Clausius–Clapeyron equation to represent equilibrium conditions between liquid water and ice. Ice pressures were initially considered but later neglected due to minor influences [74], [127], [128]. The final formulation, simplified and practical, integrates latent heat, water density, and van Genuchten SWCC parameters:

$$S_u = \left[1 + \left(\frac{-L_f \rho\omega \, ln[(T + 273.15)/273.15]}{a_v}\right)^{1/(1-m_v)}\right]^{-m_v} \quad (7)$$

Ren *et al.,* (2017) formulated a robust variant of the van Genuchten model, explicitly assuming pore-ice pressure equals atmospheric pressure and neglecting solute effects [30]. Their approach translates subzero temperatures to matric suction using the Clapeyron relationship. This gives rise to a practical and easily implementable model:

$$\theta_u = \theta_r + (\theta_s - \theta_r)\left[1 + \left(-a_v L_f \rho\omega \ln\frac{T + 273.15}{T_0 + 273.15}\right)^{n_v}\right]^{-m_v} \quad (8)$$

Zhou (2020) also adapted the classical van Genuchten formulation by directly replacing matric suction with temperature [129]. This adaptation makes the widely accepted van Genuchten SWCC applicable straightforwardly for freezing soils, capturing temperature-dependent soil water behavior explicitly:

$$\theta_u = (\theta_s - \theta_r)\left[1 + \left(-a_v(-T)\right)^{n_v}\right]^{-m_v} + \theta_r \quad (9)$$

**4.1.2 Fredlund Model**

Similar to the van Genuchten-Ren model, the Fredlund and Xing-Ren model merges the Fredlund and Xing SWCC equation with Clapeyron thermodynamics [30]. It retains the essential features of the Fredlund-Xing approach, offering flexibility and accuracy for diverse soil types through empirical fitting parameters:

$$\theta_u = \theta_s \left[ln\left(2.718 + \left(-\frac{L_f \rho\omega}{a_f} ln\frac{T + 273.15}{T_0 + 273.15}\right)^{n_f}\right)\right]^{-m_f} \quad (10)$$

Zhou (2020) [129] transformed the Fredlund and Xing SWCC model for freezing soils by replacing matric suction with negative temperature, retaining its characteristic logarithmic structure for modelling temperature-induced changes in unfrozen water content:

$$\theta_u = (\theta_s - \theta_r)\left[ln\left(e + \left(\frac{-T}{a_f}\right)^{n_f}\right)\right]^{-m_f} + \theta_r \quad (11)$$

Wen *et al.,* (2020) produced generalized formulations by replacing saturated water content with initial water content, integrating simplified Clapeyron equations [130]. These models are notable for their excellent performance and simplified computational demands, especially the Fredlund and Xing (C=1)-Wen model, which was the best-performing SWCC-based model evaluated.

**4.1.3 Pham-Zhou Model**

Zhou (2020) [129] reformulated Pham's SWCC model by substituting soil matric suction directly with subzero temperatures. It provides a direct analogy to the soil water retention behavior under freezing conditions, highlighting temperature effects explicitly:

$$\theta_u = \frac{\theta_s \alpha + \theta_r (-T)^m}{\alpha + (-T)^m} \quad (12)$$

**4.1.4 Soil-Freezing Curves Using Clausius–Clapeyron Equation**

To evaluate soil-freezing curves (SFCs) derived from the Clausius–Clapeyron (C–C) equation, an extensive dataset was compiled encompassing experimental SFCs, soil–water retention curves (SWRCs), and associated physical characteristics of sand, silt, and clay soils. These data were used to construct a comprehensive database aimed at examining the thermohydraulic behavior of different soil types under freezing conditions. To describe the soil–water retention behavior, the van Genuchten (1980) model was applied to the experimental SWRC data, represented by the following equation [122]:

$$S_r = S_{res} + (1 + S_{res})(1 + [\alpha(\psi)]^n)^{-m} \quad (13)$$

$S_r$ is the degree of saturation, $S_{res}$ is the residual saturation, ψ denotes suction in kilopascals (kPa), and α, m, and n are empirical fitting parameters. Specifically, α reflects the inverse of air-entry pressure, while mm and nn are related to the pore size distribution characteristics of the soil.

Once the SWRCs were modelled, the corresponding suction values were used to estimate the freezing temperatures of pore water by manipulating the Clausius–Clapeyron relationship. The pore-water pressure during drying, $P_w$, is related to the freezing temperature TT through the logarithmic form of the C–C equation:

$$P_{\omega f} = L_f \rho\omega \, ln\frac{T}{T_0} \approx L_f \rho\omega \frac{T - T_0}{T_0} \quad (14)$$

Rearranging gives the expression:

$$T \approx \frac{P_w}{L_f \rho\omega} T_0 - T_0 \quad (15)$$

In this formulation, $L_f$ is the latent heat of fusion of water (J/kg), $\rho\omega$ is the density of water (kg/m³), $T_0$ is the reference temperature (typically 273.15 K), and T is the estimated freezing temperature corresponding to a given pore-water pressure [122], [123].

The compiled dataset encompasses experiments conducted at the element, tank, and field scales, under freezing, thawing, and combined freeze–thaw conditions. A detailed overview of these experiments, including the nature of the geomaterials and relevant citations, is provided in Table 1. Individual case examples such as "sand #1" are used to demonstrate the comparative framework adopted for cross-analysing freezing characteristics across soil types.

**Table 1 Overview of Experimental Datasets Used to Characterize Unfrozen Water Dynamics in Various Soil Types**

| Soil Composition | Measurement Technique | Thermal Condition | Experimental Scale | Methodological Details | Reff. |
|---|---|---|---|---|---|
| Silty clay, lean clay | FDR sensor (EC-5) | Freeze–Thaw | 50 mm diameter × 100 mm height | Freezing and thawing cycles implemented in a laboratory freezer with 12 h intervals at each thermal step | [64] |
| Silt, clay | NMR | Thaw | 16 cm² cross-section, 2 cm tall | Gradual thawing from −40°C to 20°C using a thermostatic bath with dwell times between 4–10 h | [98] |
| Sandy clay, silty clay | Thermal TDR | Freeze–Thaw | Elemental level | Assessed both slow and rapid freeze/thaw rates to explore non-equilibrium water content response | [112] |
| Clayey silt, sand, silty clay | NMR | Thaw | 17.3 mm diameter × 25 mm height | Samples warmed from −20°C to 0°C, allowing 2-hour equilibrium intervals per temperature step | [97] |
| Sandy silt | TDR | Freeze | 5.3 cm diameter × 23.6 cm height | Series of tests conducted across four levels of initial saturation: frozen using Peltier plates | [106] |
| Fine silt | TDR (in situ) | Freeze | Field scale (29 cm depth) | SFC and SWRC measured from undisturbed field samples taken from depths between 30–37 cm | [110] |
| Silt, fine sand | Capacitive sensors | Freeze | 1 m × 1 m × 0.1 m test tank | Boundary-driven freezing experiment; top and bottom temperatures held constant | [107] |
| Coarse silt, fine silt, clayey silt | Dilatometer | Freeze–Thaw | 1.2 cm diameter × 4 or 10 cm height | Thermally cycled in constant-temperature bath with 24-hour dwell periods | [113] |
| Silt, sand | TDR | Thaw | 78 mm diameter × 30 mm height | Soil thawed from −4.5°C to 0°C in 1 hour with an upward water flow rate of 0.53 m/day | [96] |
| Silty sand | NMR | Freeze–Thaw | 8 cm³ volume | Experiments performed in controlled thermal bath; 45-minute intervals per thermal stage | [99] |
| Silt | TDR | Freeze | Element scale | Samples were pre-consolidated to 50 and 100 kPa and frozen in a thermostatic chamber | [99] |
| Silt | Calorimetry | Freeze | 3.81 cm diameter × 10.16 cm height | Soil freezing curve derived using thermal data from prior work by Jame and Norum (1972) | [111] |
| Silt | Calorimetry | Freeze | 120 cm³ sample | Heat flux–induced freezing from the outer wall of the container to the sample core | [94] |
| Sandy silt | TDR | Freeze–Thaw | Field setup (5 and 10 cm depths) | Hourly monitoring through the fall–winter season capturing subsurface thermal/moisture changes | [108] |

Comparisons between observed and predicted SFCs for sandy soils reveal nonlinear saturation–temperature relationships, particularly between 0°C and −1°C (Fig. 3a). While the van Genuchten model generally aligns with experimental data, it often exaggerates the transition slope, producing an abrupt decline in saturation uncharacteristic of SWRCs. For silt-based soils, model–data discrepancies are more pronounced (Fig. 3b). Samples #12, #3, and clayey silt #2 show extended freezing down to −4°C, whereas others exhibit sharp transitions, reflecting variability in pore-water thermodynamics. Azmatch *et al.,* (2012) examined overburden pressure effects

at 50 and 100 kPa, finding that C–C-based predictions overestimated freezing temperatures especially at 50 kPa due to limited suction range (~400 kPa) in SWRC calibration [108].

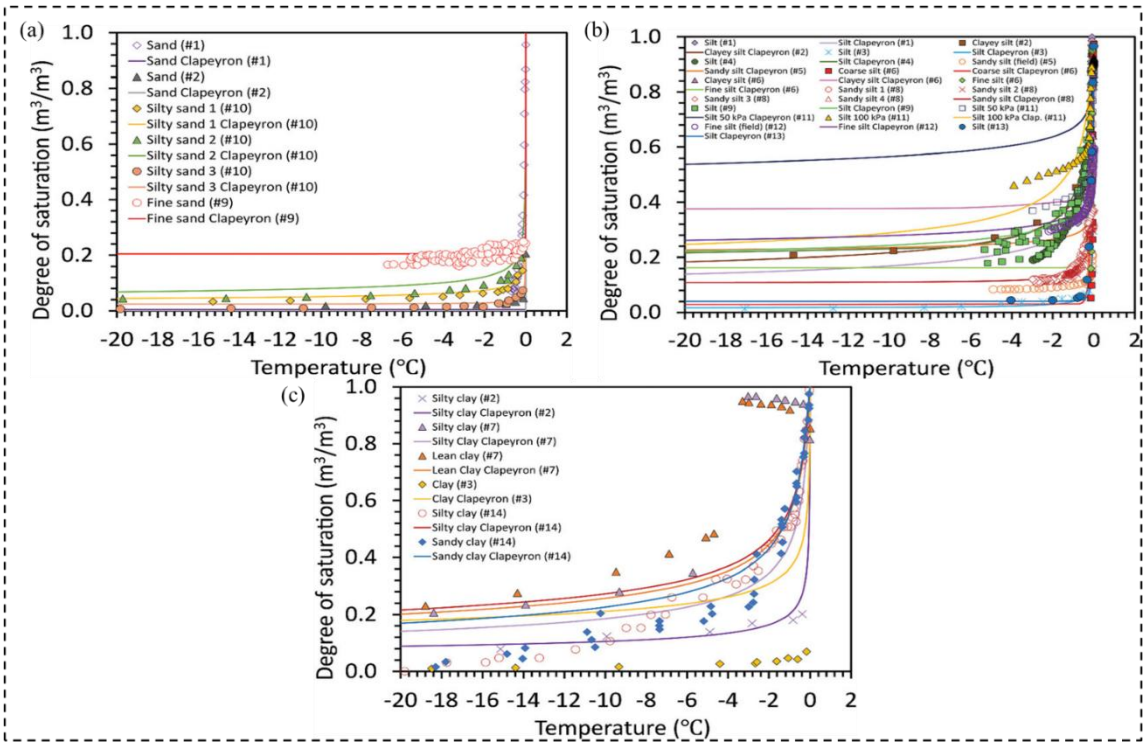


**Figure 3 SFCs for (a) Sand; (b) Silt; (c) Clay [123].**

Field data for sandy and fine silts (samples #5 and #12) highlight variations in model agreement. Fine silt exhibited better alignment with observed soil freezing curves (SFCs), likely due to its more uniform pore structure. Both studies used TDR sensors and SWRCs derived from undisturbed samples, though measurement precision varied Spaans and Baker (1996) [110] reported thermistor accuracy of ±0.005 °C, while [110] *et al.,* (2006) used ±0.15 °C sensors, with identical TDR water content error (±0.02 $m^3/m^3$). Deviations in sandy silt data may stem from sample disturbance or natural heterogeneity . Clay-rich soils exhibited delayed thermal equilibrium and more pronounced model–data mismatches below −2 °C (Fig. 3c). While some datasets (e.g., Liu *et al.,* 2012, sample #14) matched well above −2 °C, others diverged significantly due to factors like hysteresis, where drying-based SWRCs fail to reflect thawing-dominated SFCs. Additional deviations (e.g., in sample #5) were linked to supercooling effects, where water remains unfrozen below 0 °C and undergoes sudden crystallization phenomena poorly captured by traditional SWRC-based models [112].

### 4.2 Comparison of Models

Among the various SWRC-based formulations for predicting soil freezing characteristic curves, the van Genuchten (VG)-based models, particularly the Bittelli adaptation [122], [131], remain the most widely used and practically reliable. Their strength lies in the direct integration of established VG parameters with the Clausius–Clapeyron relation, allowing relatively accurate predictions across a broad range of soil textures while requiring only conventional retention curve data. The Fredlund–Xing–based models offer comparable applicability and, as shown by Wen *et al.,* perform better near the freezing point by accounting for the influence of initial water content, though their parameters are sometimes less intuitive to calibrate [130]. Other variants, such as the VG–Nishimura and VG–Zhou formulations, simplify the governing expressions but at the expense of neglecting critical effects like ice pressure, which can reduce accuracy in fine-textured soils. Empirical power-law models, while computationally simple, lack universality and fail to capture soil-specific pore-scale physics. In contrast, Gibbs–Thomson–based approaches, though theoretically rigorous and capable of incorporating pore-size distribution and salinity, are often limited by the demanding laboratory data requirements. Overall, the VG-based models strike the most effective balance between accuracy, data availability, and computational simplicity, making them the most useful in both research and applied geotechnical or permafrost engineering contexts, whereas other formulations tend to be either oversimplified or overly complex for routine applications. The comparison of these models is provided in Table 2.

**Table 2 Comparison of SWRC-based models for soil freezing characteristic curves (SFCCs).**

| Model | Formulation (compact) | Parameters & typical ranges | Data required to fit | Soils & T-range | Ice-pressure / salinity treatment | Hysteresis |
|---|---|---|---|---|---|---|
| **van Genuchten** | VG SWRC mapped to T via Clausius–Clapeyron. $\theta_u = \theta_r + (\theta_s - \theta_r)[1 + (\alpha \cdot \Phi(T))^n]^{-m}$. | $\alpha \approx 10^{-4}$–1 $kPa^{-1}$. n ≈ 1–10. m = 1−1/n. $\theta_s \approx 0.20$–0.60. $\theta_r \approx 0$–0.20. | SWRC parameters or $\theta_u$–T data. | Sands → clays; typical lab range 0 to −20 °C. | Usually neglects ice pressure; salinity not explicit. | Assumes equilibrium; no hysteresis. |
| **VG–Nishimura** | Simplified VG with C–C mapping; ice pressure considered then dropped. | Same as VG but simplified parameterization. | SWRC or $\theta_u$–T. | Silts, clays; similar T-range. | Ice pressure neglected in final use; salts not included. | Equilibrium only. |
| **VG–Zhou** | Heuristic substitution: replace suction term by (−T) scaling in VG. | VG-like α, n, m; reinterpreted for T. | Preferably $\theta_u$–T data. | Broad textures; applied to sandstones. | Ice pressure/salinity not included. | Equilibrium only. |
| **Fredlund–Xing → SFCC** | FX SWRC mapped by C–C; Wen replaces $\theta_s$ with initial water content. | $a_f$, $n_f$, $m_f$ (soil-dependent); $\theta_s \approx$ 0.20–0.60. | SWRC or $\theta_u$–T data. | Applicable to sands, silts, clays; Wen robust near 0 °C. | Ice pressure/salinity neglected. | Equilibrium only. |
| **Pham → SFCC** | Pham SWRC structure mapped to T. | α, n (soil-dependent). | $\theta_u$–T data. | Used across soil types. | No explicit ice/salinity. | Equilibrium only. |
| **Empirical / power-law** | $\theta_u = A \cdot$ | T | ^B; or PTF regressions with SSA. | A, B fitted; SSA coefficients. | Minimal: SSA, $\theta_u$–T points. | Sands and clays; moderate T ranges. |
| **Gibbs–Thomson / pore-scale** | Uses PSD + Gibbs–Thomson $\Delta T \propto 1/r$; solute freezing depression. | PSD and solute-dependent parameters. | MIP/$N_2$ adsorption, solute conc., $\theta_u$–T. | Fine-textured clays, saline soils. | Explicitly includes pore-ice pressure and salinity. | Some dynamic GT models include hysteresis. |

### 4.3 Advantages and Disadvantages of SFCC Models

#### 4.3.1 van Genuchten-Based Models

The van Genuchten (VG) model is widely recognized for its simplicity and ability to fit a broad range of soil water retention data. Its parameters are physically meaningful, representing the air-entry value and pore-size distribution, which are crucial for understanding soil-water interactions. The model's flexibility allows it to approximate various soil behaviours, making it a standard choice in many hydrological and geotechnical applications.

Despite its widespread use, the VG model has limitations when applied to frozen soils. It assumes equilibrium conditions, which may not hold during freeze-thaw cycles. Additionally, it does not account for the effects of ice pressure and salinity on the soil's water retention properties, leading to potential inaccuracies in predicting unfrozen water content at sub-zero temperatures. These shortcomings can be particularly significant in fine-textured soils and saline environments.

#### 4.3.2 Fredlund and Xing (FX) Models

The FX models offer greater flexibility by introducing additional parameters that allow for a more nuanced representation of the soil-water relationship. This flexibility enables the FX models to better capture the complexities of soil behavior under varying conditions, including the effects of freezing and thawing. They have been shown to provide improved fits to experimental data compared to simpler models.

The increased complexity of the FX models comes with the need for more extensive data for calibration, which can be a limitation in practical applications. The interpretation of the additional parameters can also be less straightforward, requiring a deeper understanding of the underlying soil processes. Furthermore, like the VG model, the FX models do not inherently account for the effects of ice pressure and salinity, which can influence the accuracy of predictions in certain soil types.

#### 4.3.3 Pham-Based Models

Pham-based models are noted for their simplicity and ease of implementation. They require fewer parameters, making them less data-intensive and more accessible for applications with limited information. This simplicity can be advantageous in large-scale modeling where computational efficiency is a priority.

The primary limitation of Pham-based models is their oversimplification of the soil-water relationship. They do not account for the complex interactions between soil particles, water, and ice, leading to less accurate predictions

of unfrozen water content, especially in soils with heterogeneous properties. Their application is generally limited to specific soil types or conditions where their assumptions hold reasonably well.

**4.3.4 Empirical Power-Law Models**

Empirical power-law models are straightforward and computationally efficient, making them suitable for quick assessments and scenarios where detailed data is unavailable. Their simplicity allows for rapid implementation in large-scale simulations.

These models lack a physical basis, relying solely on empirical relationships that may not generalize well across different soil types or conditions. They do not account for the underlying mechanisms governing soil-water interactions, such as pore structure and solute effects, leading to potential inaccuracies in predictions, particularly under varying environmental conditions.

**4.3.5 Gibbs–Thomson (GT) Models**

GT models are grounded in thermodynamic principles, providing a more fundamental understanding of the soil-water relationship. They can incorporate the effects of pore size distribution and solute concentration, offering a more detailed representation of freezing behavior in soils. This makes them particularly useful in studies of fine-textured and saline soils. The application of GT models requires detailed information about the soil's pore structure and solute content, which may not always be readily available. Their complexity can also lead to increased computational demands, making them less suitable for large-scale applications without sufficient data. Additionally, the interpretation of the model's parameters can be challenging, requiring specialized knowledge.

**Table 3 Comparative Evaluation of SFCC Models**

| Model | Equilibrium Assumption | Ice Pressure Consideration | Salinity Effects | Parameter Interpretability | Data Requirements |
|---|---|---|---|---|---|
| VG-based | ✓ | ✗ | ✗ | Moderate | Low |
| FX-based | ✓ | ✗ | ✗ | High | Moderate |
| Pham-based | ✓ | ✗ | ✗ | Low | Low |
| Power-law | ✗ | ✗ | ✗ | Low | Low |
| GT-based | ✗ | ✓ | ✓ | High | High |

## V. Hysteresis in Unfrozen Water Content During Freeze–Thaw Cycles

### 5.1 Hysteresis Characteristics of the Soil–Water System

The thermodynamic profile of the soil–water system during a typical freeze–thaw (FT) cycle is categorized into three major phases (Fig. 4): the freezing segment (depicted in blue), the isothermal phase (black), and the thawing segment (red).

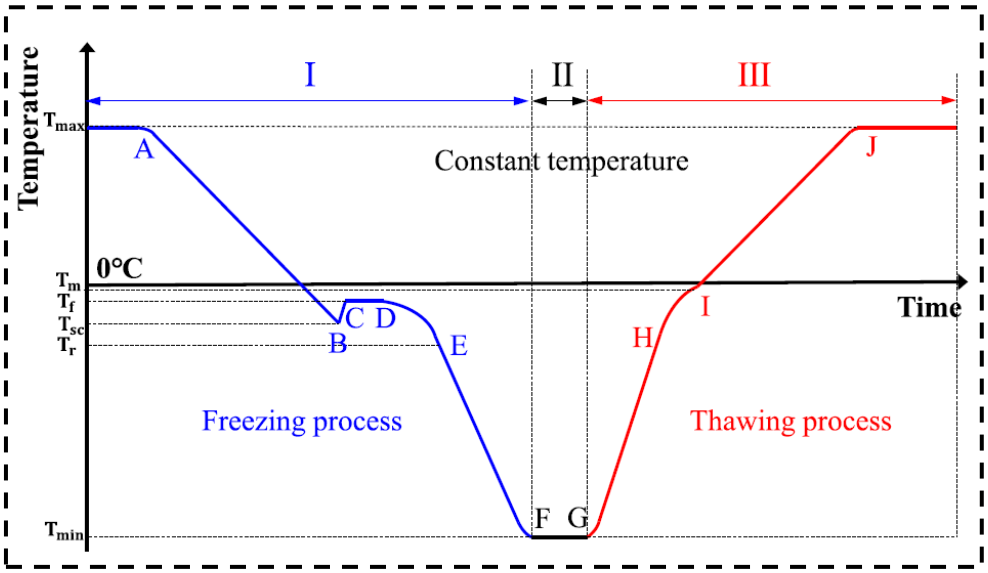


**Figure 4 Temperature–time profile of the soil–water system during a freeze–thaw cycle, illustrating key thermal points including $T_{min}$, $T_{sc}$, $T_f$, $T_r$, and $T_m$ [132].**

#### 5.1.1 Freezing Behavior of the Soil–Water Matrix

The progression of freezing, delineated by the blue segment (Fig. 6) can be further partitioned into five distinct stages AB, BC, CD, DE, and EF as described in prior studies [133], [134]. Initially, at stage AB, although the

temperature drops below 0 °C at point B, ice nucleation does not occur immediately due to the supercooling of the pore solution. In this metastable state, only a minimal population of ice crystal nuclei emerges, insufficient to induce substantial phase transition. Consequently, the specific heat capacity of the system remains effectively constant, assuming negligible temperature dependence. Under consistent external heat exchange, this leads to a linear decrease in temperature, rendering the AB segment nearly straight with a negative slope.

The BC phase marks the nucleation burst. As the system cools further, it surpasses the threshold energy barrier for spontaneous crystallization. Rapid ice formation ensues, releasing latent heat and causing a transient rise in temperature. This interval, typically brief, is characterized by a steep, nearly linear increase in temperature. In stage CD, the system enters a quasi-equilibrium condition where the rate of heat extraction matches the latent heat released during the ice formation process. As a result, the temperature stabilizes, forming a plateau in the curve. During this stage, freezing primarily involves the conversion of free and capillary water into ice. Subsequently, stage DE reflects renewed cooling. As freezing extends to more strongly bound water fractions particularly adsorbed water the rate of phase change slows. Simultaneously, the accumulation of ice within pore spaces alters the system's heat capacity; specifically, the specific heat of ice is lower than that of water. This thermal property shift enhances the cooling rate, producing a curved segment with a progressively steeper negative gradient.

In the final cooling phase EF, the remaining unfrozen moisture mostly strongly adsorbed water remains in a non-crystalline state due to the high adsorption potential of soil mineral surfaces [135], [136]. With negligible ongoing phase change and consistent heat exchange, the specific heat remains unchanged, rendering this segment linear with a smaller negative slope compared to AB. This slope difference arises because ice possesses a specific heat capacity approximately half that of water [137].

The thermal trajectory during the freezing process is governed by three principal factors: the rate of phase transformation, the ambient cooling rate, and the system's average specific heat. The ambient cooling rate dictates the energy flux to and from the system, while the phase transition rate controls the dynamics of latent heat release or absorption. The average specific heat, in turn, is modulated by the unfrozen water content at each stage. When the soil system undergoes purely sensible heat changes such as during AB and IJ without phase transitions, the specific heat remains nearly constant. In contrast, during segments involving significant water-to-ice transformations (e.g., BC to DE), the specific heat evolves dynamically. Notably, in both the EF and GH segments, the freezing or thawing process is nearly complete, and thus the system's specific heat remains stable again. Since the mass contributions of pore gases are minor and soil particles do not participate in phase change, the major influence on specific heat stems from moisture transitions. As liquid water solidifies, the system's specific heat drops markedly, underscoring the relationship between initial water content and the temperature curve's slope during segments AB and EF.

### 5.1.2 Thawing Dynamics of the Soil–Water System

The thawing phase (Fig. 5) comprises three stages GH, HI, and IJ based on the framework by Xu *et al.,* (2010) [138]. Initially, during GH, no phase transformation takes place. The system's ice content remains unaltered as temperature increases. The specific heat thus remains constant, resulting in a linear temperature rise under uniform external heat input.

The following HI stage captures the phase transition from ice to liquid water. As pore ice begins to melt, the released heat from the heating element is absorbed by the system, increasing the water content and thereby elevating the system's overall specific heat. Because water has a higher specific heat than ice, the temperature rise becomes increasingly subdued, producing a curved trajectory with a gradually diminishing slope. Finally, during segment IJ, the ice has fully melted into water. The system stabilizes thermally, and with no ongoing phase transition, the specific heat remains fixed. Under steady energy input, this stage follows a linear increase in temperature. However, the slope is gentler than that of GH, reflecting the higher specific heat of the water-dominated system compared to its ice-dominated counterpart [139].

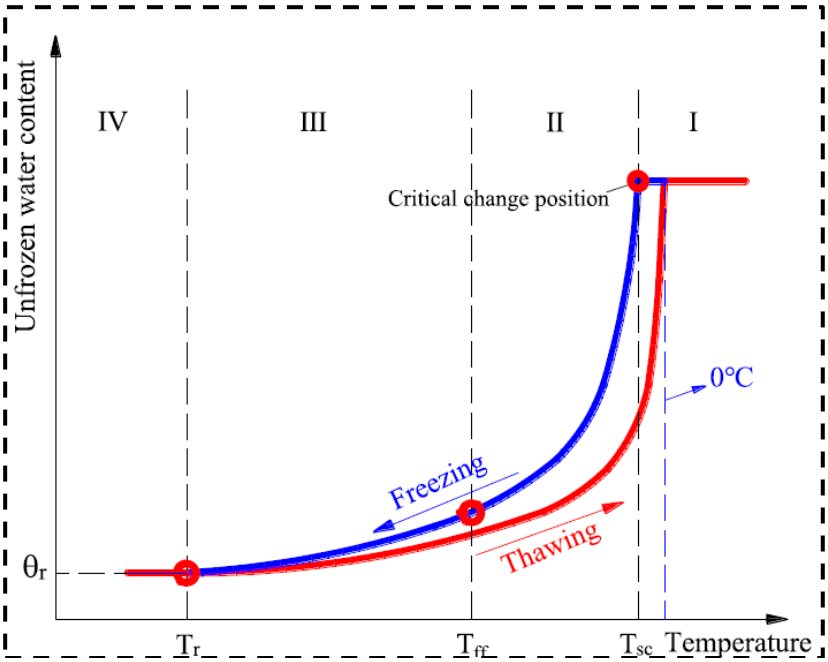


**Figure 5 Unfrozen water content variation with temperature during a freeze–thaw cycle, indicating $T_{ff}$ as the complete freezing point of free water in soil [138].**

### 5.2 Hysteresis Phenomena During Cyclic Conditions

The soil-freezing and thawing behavior of sands and clays was examined using experimental data alongside soil-freezing curves (SFCs) derived from the soil–water retention curves (SWRCs) (Fig. 6). A key limitation of the Clausius–Clapeyron (C–C) equation hysteresis was clearly observed in the case of #7 lean clay and silty clay. This hysteresis arises primarily from the phenomenon of supercooling, where pore water remains unfrozen at subzero temperatures due to the combined effects of capillary and adsorption forces. However, when experiments are designed to eliminate supercooling, such hysteresis is not observed. For example, the #10 silty sand showed a much lower degree of hysteresis in its freeze–thaw response compared to clays. Despite this, a slight difference remains, where the thawing curve tends to indicate a slightly lower saturation than during freezing an effect likely caused by microstructural changes in the soil matrix during the freeze–thaw process [123].

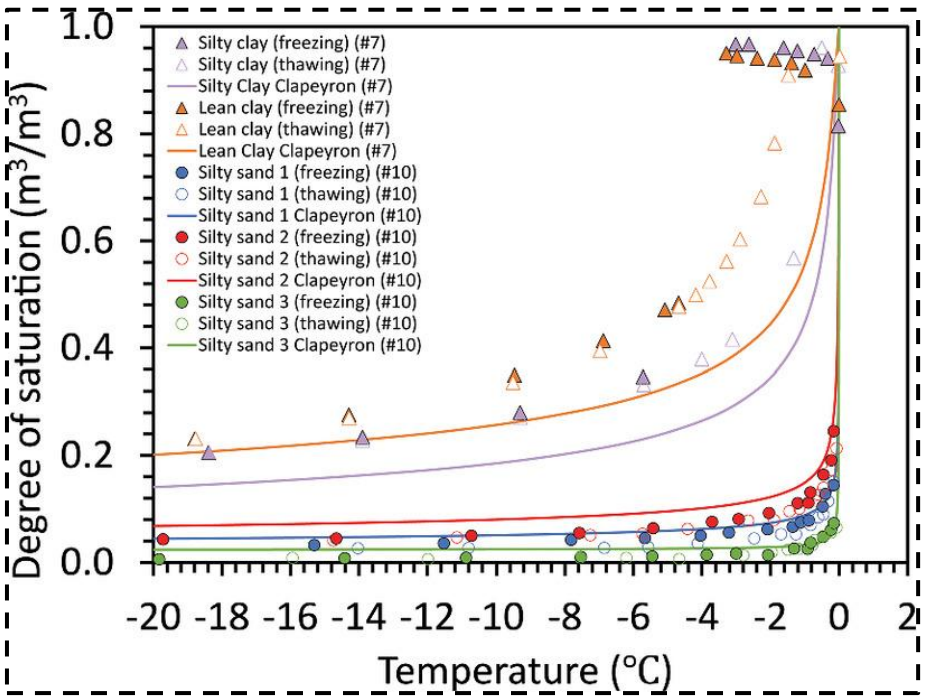


**Figure 6 Freeze–thaw hysteresis loops illustrating the unfrozen water behavior in clay and sandy soils [123].**

**5.2.1 Laboratory Freeze–Thaw Experiments**

To overcome the shortcomings associated with the C–C equation, laboratory freeze–thaw experiments were carried out using compacted Bonny silt. The soil was sieved through a #10 mesh, oven-dried for 24 hours, rehydrated with deionized water, and allowed to equilibrate for another 24 hours before testing. It was then compacted in three layers using a 10-pound modified Proctor hammer within a metal mold measuring 41.9 cm by 8.2 cm and 11.3 cm in height. To prevent moisture loss, the mold was sealed with plastic wrap following compaction.

To minimize expansion caused by frost action, boundary conditions were controlled using rigid plates and clamps, allowing expansion only in the vertical direction. Measurements of suction, unfrozen water content, and temperature were continuously recorded every 5 minutes using TEROS 21 sensors (for water potential and temperature) and TEROS 11 sensors (for volumetric water content and temperature), both produced by METER Group, Inc., Pullman, WA. The freezing phase initiated by placing the soil-filled containers inside a General Electric Manual Defrost Upright Freezer maintained at −16 °C (Fig. 7a, b). Once thermal and moisture equilibrium was achieved, the samples were brought to room temperature (21 °C) to facilitate thawing. To investigate cyclic behavior, two additional freeze–thaw cycles were subsequently applied using the same temperature gradient. The peak freezing rate observed was −2.5 °C per hour, while the maximum thawing rate reached 11.7 °C per hour.

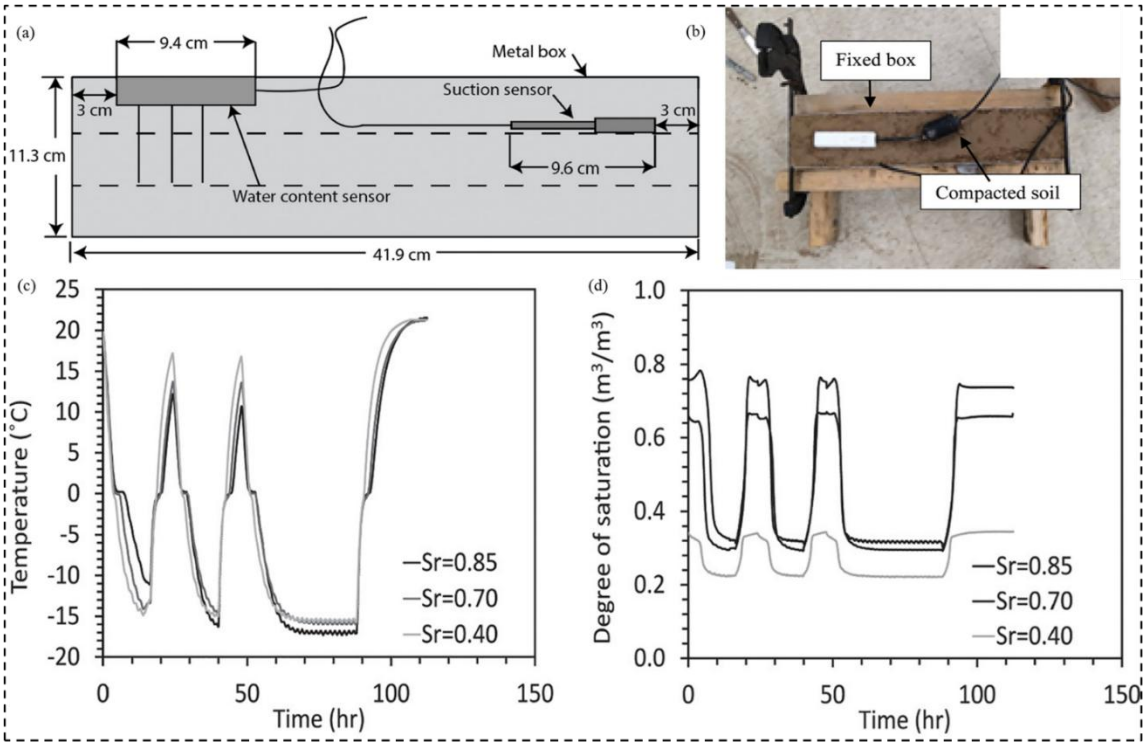


**Figure 7 Experimental freeze–thaw setup showing (a) sensor configuration and (b) top view layout. Time series data across all cycles for (c) temperature variation and (d) changes in degree of saturation [106], [123].**

Laboratory-derived SFCs for Bonny silt with initial saturations of 0.4, 0.7, and 0.85 captured both freezing and thawing responses (Fig. 8a–c). The steepest drop in unfrozen water content occurred between −2°C and −4°C, while thawing showed a more gradual rise between 1°C and 5°C demonstrating clear freeze–thaw-induced hydraulic hysteresis. This hysteresis likely results from multiple factors, including particle aggregation due to the absence of confining pressure, which may have altered pore geometry. As Watanabe *et al.,* (2012) noted, thermal equilibrium precedes hydraulic equilibrium, delaying saturation changes during thawing [140]. Supercooling, as described by Ren and Vanapalli (2019), also contributes by allowing water to remain unfrozen below 0°C [64]. These results further highlight the role of initial saturation: while Zhou *et al.,* (2014) suggested residual $\theta_u$ is independent of total water content, the present findings indicate a more complex dependence [106].

To assess this, the progression of the degree of saturation with respect to temperature was compared between the first and third freeze–thaw cycles (Fig. 8d-f). The Bonny silt specimens were prepared in two distinct hydraulic states: a funicular regime with Sr = 0.40, and a capillary regime with Sr = 0.70 and 0.85. Specimens compacted in the capillary state, where water exists as a continuous phase, exhibited similar freezing behaviours and converged toward a residual degree of saturation around 0.3 by the end of each cycle. In contrast, the sample

initiated at Sr=0.4 in the funicular regime consistently reached a lower residual saturation value of approximately 0.1 [123]. This outcome was repeatable across all cycles and is unlikely to be attributed to procedural inconsistencies during sample preparation, indicating a genuine influence of initial saturation regime on residual unfrozen water behavior.

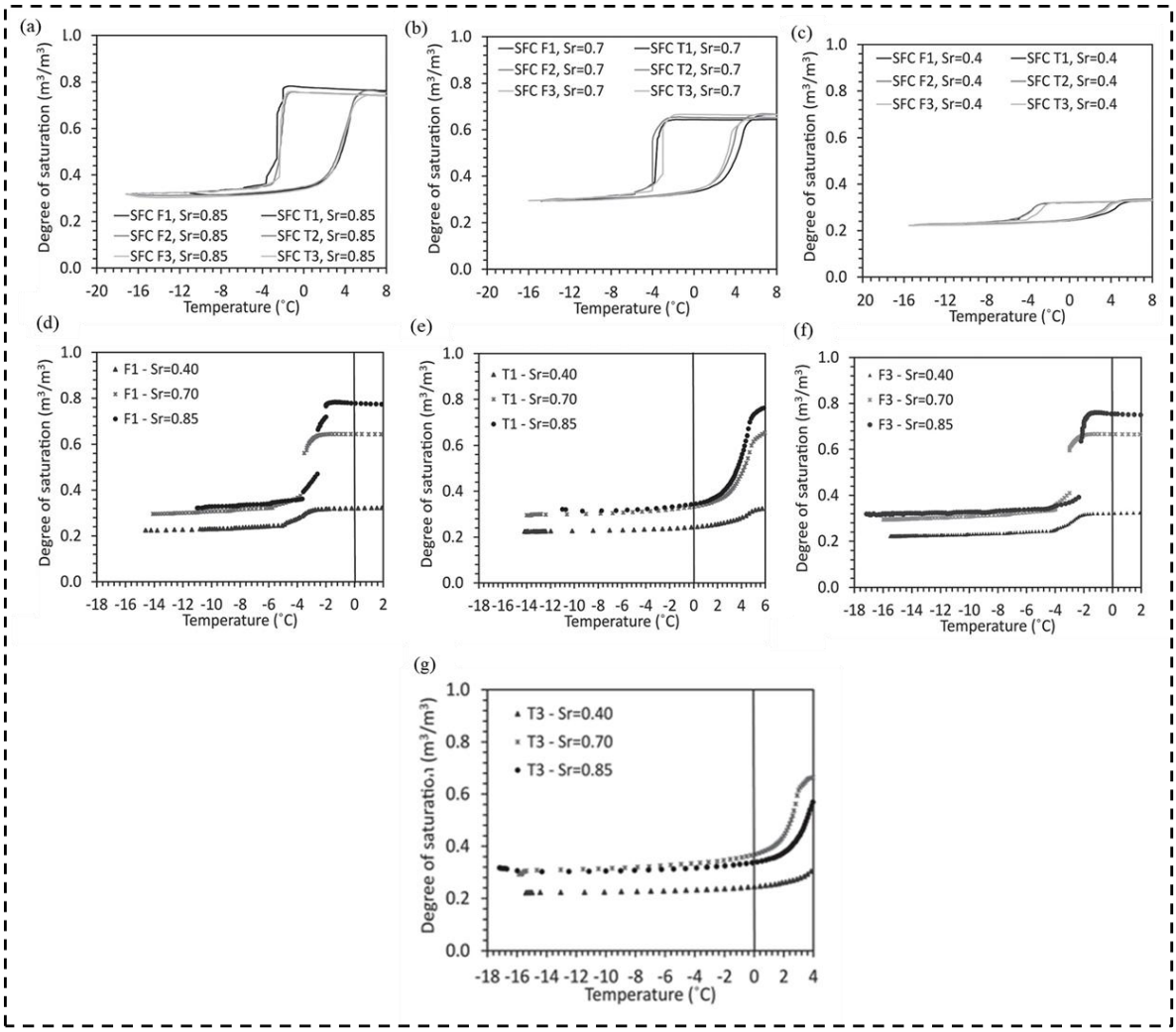


**Figure 8** Experimentally obtained soil-freezing curves for Bonny silt at varying initial saturation levels: **(a)** Sr = 0.85, **(b)** Sr = 0.7, and **(c)** Sr = 0.4. Influence of initial saturation on soil-freezing behavior across different freeze–thaw phases: **(d)** initial freezing cycle, **(e)** initial thawing cycle, **(f)** third freezing cycle, and **(g)** third thawing cycle [123].

## VI. Conclusion and Outlook

Understanding the behavior of unfrozen water in frozen soils requires a comprehensive grasp of the thermodynamic principles that govern phase transitions during freeze–thaw cycles. These transitions are highly sensitive to soil microstructure, mineralogy, and pore-size distribution. Unfrozen water persists below freezing due to adsorption, capillarity, and solute concentration, giving rise to distinct soil-freezing curves. Particularly in the narrow thermal window between −1 °C and −4 °C, the freezing process becomes nonlinear and often irreversible upon thawing. Such hysteresis is strongly influenced by mechanisms such as particle aggregation, structural rearrangement, and the lag between thermal and hydraulic responses.

Recent progress in experimental methods, notably low-field nuclear magnetic resonance, time-domain reflectometry, and cryogenic thermal analysis, has enabled more accurate quantification of bulk, capillary, and bound water content. These advancements have expanded the measurable temperature range and improved resolution in detecting phase changes. Nonetheless, challenges remain in calibration under cryogenic conditions and in capturing dynamic changes during repeated freeze–thaw cycling. Predictive models, particularly those based on thermodynamic analogies such as the Clausius–Clapeyron equation, often fall short in representing the smooth transitions and hysteretic effects observed in real soils. Limitations in capturing the influence of pore-scale heterogeneity, initial saturation states, and non-equilibrium behavior further reduce model reliability.

Looking forward, improving prediction and measurement of unfrozen water content requires the integration of microstructural soil properties into thermohydraulic models. Standardizing freezing protocols and expanding the use of in situ and imaging-based techniques will be crucial for reconciling laboratory and field-scale discrepancies. Addressing lag effects, hysteresis, and scaling issues is key to developing robust models capable of simulating freeze–thaw processes across soil types and environmental conditions. With these refinements, future studies will be better positioned to assess the impacts of freezing on infrastructure, hydrological processes, and climate-sensitive geotechnical systems.

## References

[1] C. Lyu, S. A. G. Amiri, G. Grimstad, K. V. Høyland, and T. Ingeman-Nielsen, 'Comparison of Geoacoustic Models for Unfrozen Water Content Estimation', *J. Geophys. Res. Solid Earth*, vol. 125, no. 10, 2020, doi: 10.1029/2020JB019766.
[2] F. Ming, L. Chen, D. Li, and X. Wei, 'Estimation of hydraulic conductivity of saturated frozen soil from the soil freezing characteristic curve', *Sci. Total Environ.*, vol. 698, 2020, doi: 10.1016/j.scitotenv.2019.134132.
[3] T. Kozlowski, 'A simple method of obtaining the soil freezing point depression, the unfrozen water content and the pore size distribution curves from the DSC peak maximum temperature', *Cold Reg. Sci. Technol.*, vol. 122, pp. 18–25, 2016, doi: 10.1016/j.coldregions.2015.10.009.
[4] Y. Lai, W. Wen, W. Pei, and X. Wan, 'A novel transport model to predict the moisture-heat-gas-salt behavior in unsaturated saline soil under evaporation', *J. Hydrol.*, vol. 603, 2021, doi: 10.1016/j.jhydrol.2021.127052.
[5] B. L. Kurylyk and K. Watanabe, 'The mathematical representation of freezing and thawing processes in variably-saturated, non-deformable soils', *Adv. Water Resour.*, vol. 60, pp. 160–177, 2013, doi: 10.1016/j.advwatres.2013.07.016.
[6] W. Dobiński, 'Permafrost active layer', *Earth-Science Rev.*, vol. 208, 2020, doi: 10.1016/j.earscirev.2020.103301.
[7] R. Pardo Lara, A. A. Berg, J. Warland, and E. Tetlock, 'In Situ Estimates of Freezing/Melting Point Depression in Agricultural Soils Using Permittivity and Temperature Measurements', *Water Resour. Res.*, vol. 56, no. 5, 2020, doi: 10.1029/2019WR026020.
[8] J. Zhou, X. Meng, C. Wei, and W. Pei, 'Unified Soil Freezing Characteristic for Variably-Saturated Saline Soils', *Water Resour. Res.*, vol. 56, no. 7, 2020, doi: 10.1029/2019WR026648.
[9] L. Kang *et al.*, 'Metagenomic insights into microbial community structure and metabolism in alpine permafrost on the Tibetan Plateau', *Nat. Commun.*, vol. 15, no. 1, 2024, doi: 10.1038/s41467-024-50276-2.
[10] T. Chang *et al.*, 'Unraveling the non-linear relationship between seasonal deformation and permafrost active layer thickness', *npj Clim. Atmos. Sci.*, vol. 7, no. 1, 2024, doi: 10.1038/s41612-024-00866-0.
[11] F. Xu, J. Chen, and W. L. Jin, 'Experimental investigation of concrete-filled steel tubular longitudinal gusset plate connections', *J. Constr. Steel Res.*, vol. 124, pp. 163–172, 2016, doi: 10.1016/j.jcsr.2016.04.019.
[12] S. Ge, J. McKenzie, C. Voss, and Q. Wu, 'Exchange of groundwater and surface-water mediated by permafrost response to seasonal and long term air temperature variation', *Geophys. Res. Lett.*, vol. 38, no. 14, 2011, doi: 10.1029/2011GL047911.
[13] Y. Iwata, M. Hayashi, S. Suzuki, T. Hirota, and S. Hasegawa, 'Effects of snow cover on soil freezing, water movement, and snowmelt infiltration: A paired plot experiment', *Water Resour. Res.*, vol. 46, no. 9, 2010, doi: 10.1029/2009WR008070.
[14] E. Poutou, G. Krinner, C. Genthon, and N. de Noblet-Ducoudré, 'Role of soil freezing in future boreal climate change', *Clim. Dyn.*, vol. 23, no. 6, pp. 621–639, 2004, doi: 10.1007/s00382-004-0459-0.
[15] R. Li *et al.*, 'Soil thermal conductivity and its influencing factors at the Tanggula permafrost region on the Qinghai–Tibet Plateau', *Agric. For. Meteorol.*, vol. 264, pp. 235–246, 2019, doi: 10.1016/j.agrformet.2018.10.011.
[16] D. J. Nicolsky, V. E. Romanovsky, and G. G. Panteleev, 'Estimation of soil thermal properties using in-situ temperature measurements in the active layer and permafrost', *Cold Reg. Sci. Technol.*, vol. 55, no. 1, pp. 120–129, 2009, doi: 10.1016/j.coldregions.2008.03.003.
[17] C. Grenier *et al.*, 'Groundwater flow and heat transport for systems undergoing freeze-thaw: Intercomparison of numerical simulators for 2D test cases', *Adv. Water Resour.*, vol. 114, pp. 196–218, 2018, doi: 10.1016/j.advwatres.2018.02.001.
[18] M. A. Walvoord and B. L. Kurylyk, 'Hydrologic Impacts of Thawing Permafrost—A Review', *Vadose Zo. J.*, vol. 15, no. 6, pp. 1–20, 2016, doi: 10.2136/vzj2016.01.0010.
[19] D. White *et al.*, 'The arctic freshwater system: Changes and impacts', *J. Geophys. Res. Biogeosciences*, vol. 112, no. 4, 2007, doi: 10.1029/2006jg000353.
[20] J. Qi, S. Li, Q. Yang, Z. Xing, and F. R. Meng, 'SWAT Setup with Long-Term Detailed Landuse and Management Records and Modification for a Micro-Watershed Influenced by Freeze-Thaw Cycles', *Water Resour. Manag.*, vol. 31, no. 12, pp. 3953–3974, 2017, doi: 10.1007/s11269-017-1718-2.
[21] A. M. Ireson, G. van der Kamp, G. Ferguson, U. Nachshon, and H. S. Wheater, 'Hydrogeological processes in seasonally frozen northern latitudes: Understanding, gaps and challenges', *Hydrogeol. J.*, vol. 21, no. 1, pp. 53–66, 2013, doi: 10.1007/s10040-012-0916-5.
[22] Z. Li *et al.*, 'Comparative study of the soil thermal regime in arid and semi-humid areas', *Environ. Earth Sci.*, vol. 76, no. 1, 2017, doi: 10.1007/s12665-016-6354-2.
[23] H. Singh, 'Physical model testing of piles in thawing soils subjected to single and combined loadings', 2022.
[24] G. Britteney, 'Examining Hydrogeological Processes in Freezing Soils using Remote Geophysical and Numerical Techniques', 2019. [Online]. Available: https://library-archives.canada.ca/eng/services/services libraries/theses/Pages/item.aspx?idNumber=1099580347
[25] D. M. Anderson, 'The Latent Heat of Freezing Soil Water', in *Proceedings of the International Permafrost Conference*, 1963, pp. 238–239.
[26] Q. Li, J. Song, F. Besenbacher, and M. Dong, 'Two-Dimensional Material Confined Water', *Acc. Chem. Res.*, vol. 48, no. 1, pp. 119–127, 2015, doi: 10.1021/ar500306w.
[27] R. Tycko, 'NMR at low and ultralow temperatures', *Acc. Chem. Res.*, vol. 46, no. 9, pp. 1923–1932, 2013, doi: 10.1021/ar300358z.
[28] F. Ming, D. qing Li, and Y. hang Liu, 'A predictive model of unfrozen water content including the influence of pressure', *Permafr. Periglac. Process.*, vol. 31, no. 1, pp. 213–222, 2020, doi: 10.1002/ppp.2037.
[29] B. Li, L. Huang, X. Lv, and Y. Ren, 'Variation features of unfrozen water content of water-saturated coal under low freezing temperature', *Sci. Rep.*, vol. 11, no. 1, 2021, doi: 10.1038/s41598-021-94943-6.
[30] J. Ren, S. K. Vanapalli, and Z. Han, 'Soil freezing process and different expressions for the soil-freezing characteristic curve', *Sci. Cold Arid Reg.*, vol. 9, no. 3, pp. 221–228, 2017, doi: 10.3724/SP.J.1226.2017.00221.
[31] D. M. Anderson and A. R. Tice, 'Predicting Unfrozen Water Contents in Frozen Soils From Surface Area Measurements.', *Highw Res Rec*, no. 39, pp. 12–18, 1972.
[32] R. Bai, Y. Lai, M. Zhang, and F. Yu, 'Theory and application of a novel soil freezing characteristic curve', *Appl. Therm. Eng.*, vol.

129, pp. 1106–1114, 2018, doi: 10.1016/j.applthermaleng.2017.10.121.
[33] J. Zhou, C. Wei, Y. Lai, H. Wei, and H. Tian, 'Application of the Generalized Clapeyron Equation to Freezing Point Depression and Unfrozen Water Content', *Water Resour. Res.*, vol. 54, no. 11, pp. 9412–9431, 2018, doi: 10.1029/2018WR023221.
[34] C. Wang, Y. Lai, and M. Zhang, 'Estimating soil freezing characteristic curve based on pore-size distribution', *Appl. Therm. Eng.*, vol. 124, pp. 1049–1060, 2017, doi: 10.1016/j.applthermaleng.2017.06.006.
[35] K. Watanabe and M. Mizoguchi, 'Amount of unfrozen water in frozen porous media saturated with solution', *Cold Reg. Sci. Technol.*, vol. 34, no. 2, pp. 103–110, 2002, doi: 10.1016/S0165-232X(01)00063-5.
[36] J. G. Dash, 'Thermomolecular pressure in surface melting: Motivation for frost heave', *Science (80-. ).*, vol. 246, no. 4937, pp. 1591–1593, 1989, doi: 10.1126/science.246.4937.1591.
[37] T. Kozlowski, 'A semi-empirical model for phase composition of water in clay-water systems', *Cold Reg. Sci. Technol.*, vol. 49, no. 3, pp. 226–236, 2007, doi: 10.1016/j.coldregions.2007.03.013.
[38] M. Chai, J. Zhang, H. Zhang, Y. Mu, G. Sun, and Z. Yin, 'A method for calculating unfrozen water content of silty clay with consideration of freezing point', *Appl. Clay Sci.*, vol. 161, pp. 474–481, 2018, doi: 10.1016/j.clay.2018.05.015.
[39] C. Wang, S. yang Li, X. jia He, Q. Chen, H. Zhang, and X. yu Liu, 'Improved prediction of water retention characteristic based on soil gradation and clay fraction', *Geoderma*, vol. 404, 2021, doi: 10.1016/j.geoderma.2021.115293.
[40] C. Xiao-fei, D. Yang, M. Wei, Z. Yu-long, L. Hong-sheng, and X. Xiao-zu, 'Effect of soil nutrient on the characteristic curves of soil freezing and thawing', *J. Glaciol. Geocryol.*, vol. 26, no. 4, pp. 440–448, 2004, doi: https://doi.org/10.7522/j.issn.1000-0240.2004.0072.
[41] ZHANG Xiyin, ZHANG Mingyi, LU Jianguo, PEI Wansheng, and YAN Zhongrui, 'Study of the freezing and thawing features of soil:current situation and outlook', *J. Glaciol. Geocryol.*, vol. 38, no. 6, pp. 1644–1657, 2016.
[42] L. J. S. Halloran, G. C. Rau, and M. S. Andersen, 'Heat as a tracer to quantify processes and properties in the vadose zone: A review', *Earth-Science Rev.*, vol. 159, pp. 358–373, 2016, doi: 10.1016/j.earscirev.2016.06.009.
[43] Q. Cheng, Y. Sun, X. Xue, and J. Guo, 'In Situ Determination of Soil Freezing Characteristics for Estimation of Soil Moisture Characteristics using a Dielectric Tube Sensor', *Soil Sci. Soc. Am. J.*, vol. 78, no. 1, pp. 133–138, 2014, doi: 10.2136/sssaj2013.03.0120n.
[44] H. Tian, C. Wei, H. Wei, and J. Zhou, 'Freezing and thawing characteristics of frozen soils: Bound water content and hysteresis phenomenon', *Cold Reg. Sci. Technol.*, vol. 103, pp. 74–81, 2014, doi: 10.1016/j.coldregions.2014.03.007.
[45] A. Fabbri, T. Fen-Chong, A. Azouni, and J.-F. Thimus, 'Investigation of Water to Ice Phase Change in Porous Media by Ultrasonic and Dielectric Measurements', *J. Cold Reg. Eng.*, vol. 23, no. 2, pp. 69–90, 2009, doi: 10.1061/(asce)0887-381x(2009)23:2(69).
[46] W. Huang, X. Mao, Q. Wu, and L. Chen, 'Experimental study on shear characteristics of the silty clay soil-ice interface', *Sci. Rep.*, vol. 12, no. 1, 2022, doi: 10.1038/s41598-022-23086-z.
[47] J. Kim, A. H. Lee, and W. Chang, 'Manipulation of Unfrozen Water Retention for Enhancing Petroleum Hydrocarbon Biodegradation in Seasonally Freezing and Frozen Soil', *Environ. Sci. Technol.*, vol. 55, no. 13, pp. 9172–9180, 2021, doi: 10.1021/acs.est.0c07502.
[48] N. Ali, M. Metwally, M. Elsawwaf, and A. Nazir, 'Comprehensive analysis of thermo-mechanical responses in collapsible soil under varied water content conditions', *J. Therm. Anal. Calorim.*, vol. 149, no. 23, pp. 13721–13735, 2024, doi: 10.1007/s10973-024-13439-3.
[49] E. Nartowska and T. Kozłowski, 'The Effect of Freeze-Thaw Cycling and the Initial Mass of Water on the Unfrozen Water Content of Calcium Bentonites Modified by Copper Ions', *Minerals*, vol. 12, no. 1, 2022, doi: 10.3390/min12010066.
[50] S. F. Zheng, X. Li, Y. X. Zhao, M. Wang, and X. K. Li, 'Comparative study of unfrozen water content measurement principles and calculation methods based on NMR', *Cold Reg. Sci. Technol.*, vol. 226, 2024, doi: 10.1016/j.coldregions.2024.104255.
[51] W. Zhang, H. Lei, L. Wang, Y. Bo, and C. Zhan, 'Investigation and prediction on the freezing point of the clay under different salinity conditions', *Bull. Eng. Geol. Environ.*, vol. 83, no. 8, 2024, doi: 10.1007/s10064-024-03832-5.
[52] Y. L. Chen *et al.*, 'Distinct microbial communities in the active and permafrost layers on the Tibetan Plateau', *Mol. Ecol.*, vol. 26, no. 23, pp. 6608–6620, 2017, doi: 10.1111/mec.14396.
[53] M. Chai and J. Zhang, 'Improvement of compressibility and thaw-settlement properties of warm and ice-rich frozen soil with cement and additives', *Materials (Basel).*, vol. 12, no. 7, 2019, doi: 10.3390/ma12071068.
[54] Y. Cheng, Z. Wang, S. Liang, A. Zheng, and K. Liu, 'Analysis of macro and micro freezing characteristics of gravelly soil', *Environ. Res.*, vol. 216, 2023, doi: 10.1016/j.envres.2022.114600.
[55] J. R. Espinosa, C. Navarro, E. Sanz, C. Valeriani, and C. Vega, 'On the time required to freeze water', *J. Chem. Phys.*, vol. 145, no. 21, 2016, doi: 10.1063/1.4965427.
[56] M. Vasheghani Farahani, A. Hassanpouryouzband, J. Yang, and B. Tohidi, 'Heat Transfer in Unfrozen and Frozen Porous Media: Experimental Measurement and Pore-Scale Modeling', *Water Resour. Res.*, vol. 56, no. 9, 2020, doi: 10.1029/2020WR027885.
[57] B. Li, L. Li, L. Huang, and X. Lv, 'The temperature field evolution and water migration law of coal under low-temperature freezing conditions', *Int. J. Environ. Res. Public Health*, vol. 18, no. 24, 2021, doi: 10.3390/ijerph182413188.
[58] Z. Li, J. Chen, and C. Mao, 'Experimental and theoretical investigations of the constitutive relations of artificial frozen silty clay', *Materials (Basel).*, vol. 12, no. 19, 2019, doi: 10.3390/ma12193159.
[59] V. L. Mironov, A. Y. Karavayskiy, Y. I. Lukin, and E. I. Pogoreltsev, 'Joint studies of water phase transitions in Na-bentonite clay by calorimetric and dielectric methods', *Cold Reg. Sci. Technol.*, vol. 153, pp. 172–180, 2018, doi: 10.1016/j.coldregions.2018.04.010.
[60] E. Nartowska, M. Kanuchova, and Ľ. Kozáková, 'Assessment of Unfrozen Water Content in Copper Bentonites Using the 1H NMR Technique: Optimization, the Method's Limitation, and Comparative Analysis with DSC', *Materials (Basel).*, vol. 16, no. 24, 2023, doi: 10.3390/ma16247577.
[61] E. Nartowska and T. Kozłowski, 'The Effect of the Concentration of Copper Ions on the Unfrozen Water Content in Bentonites Measured with the Use of DSC Method', *Minerals*, vol. 12, no. 5, 2022, doi: 10.3390/min12050632.
[62] R. L. Michalowski and M. Zhu, 'Frost heave modelling using porosity rate function', *Int. J. Numer. Anal. Methods Geomech.*, vol. 30, no. 8, pp. 703–722, 2006, doi: 10.1002/nag.497.
[63] J. Tan, Z. Shen, L. Xu, H. Zhang, and Y. He, 'Experimental Investigation on Seepage Characteristics of Clay–Structure Interface after Shear Deformation', *Materials (Basel).*, vol. 15, no. 11, 2022, doi: 10.3390/ma15113802.
[64] J. Ren and S. K. Vanapalli, 'Comparison of Soil-Freezing and Soil-Water Characteristic Curves of Two Canadian Soils', *Vadose Zo. J.*, vol. 18, no. 1, pp. 1–14, 2019, doi: 10.2136/vzj2018.10.0185.
[65] S. Tian, L. Tang, X. Ling, S. Li, X. Kong, and G. Zhou, 'Experimental and analytical investigation of the dynamic behavior of granular base course materials used for China's high-speed railways subjected to freeze-thaw cycles', *Cold Reg. Sci. Technol.*, vol. 157, pp. 139–148, 2019, doi: 10.1016/j.coldregions.2018.10.003.
[66] Y. Tobo, 'An improved approach for measuring immersion freezing in large droplets over a wide temperature range', *Sci. Rep.*, vol. 6, 2016, doi: 10.1038/srep32930.
[67] X. Wan, D. Tan, Y. Lai, S. Li, J. Lu, and Z. Yan, 'Experimental study on pore water phase transition in saline soils', *Cold Reg. Sci.*

*Technol.*, vol. 203, 2022, doi: 10.1016/j.coldregions.2022.103661.
[68] W. Wang *et al.*, 'Hydrochemical characteristics of ground ice in permafrost regions of the Qinghai-Tibet Plateau', *Sci. Total Environ.*, vol. 626, pp. 366–376, 2018, doi: 10.1016/j.scitotenv.2018.01.097.
[69] C. Wang, S. Li, T. Zhang, and Z. You, 'Experimental study on mechanical characteristics and fracture patterns of unfrozen/freezing saturated coal and sandstone', *Materials (Basel).*, vol. 12, no. 6, 2019, doi: 10.3390/ma12060992.
[70] Z. Chen, J. Rao, and Y. Wan, 'The Effect of Temperature Pathways on Unfrozen Water and Thermal Parameters of Frozen Soils', *Soil Mech. Found. Eng.*, vol. 61, no. 3, pp. 257–263, 2024, doi: 10.1007/s11204-024-09970-y.
[71] H. Wang, Y. Wu, M. Wang, and X. Li, 'Influence of fines content and degree of saturation on the freezing deformation characteristics of unsaturated soils', *Cold Reg. Sci. Technol.*, vol. 201, 2022, doi: 10.1016/j.coldregions.2022.103610.
[72] J. W. Zhang, Q. Y. Mu, H. J. Liao, and F. L. Liu, 'A soil freezing characteristic curve model for capturing void ratio and specific surface area effects', *Yantu Lixue/Rock Soil Mech.*, vol. 41, no. 9, pp. 2913–2921, 2020, doi: 10.16285/j.rsm.2019.1982.
[73] A. M. Kruse and M. M. Darrow, 'Adsorbed cation effects on unfrozen water in fine-grained frozen soil measured using pulsed nuclear magnetic resonance', *Cold Reg. Sci. Technol.*, vol. 142, pp. 42–54, 2017, doi: 10.1016/j.coldregions.2017.07.006.
[74] Q. Y. Mu, C. W. W. Ng, C. Zhou, G. G. D. Zhou, and H. J. Liao, 'A new model for capturing void ratio-dependent unfrozen water characteristics curves', *Comput. Geotech.*, vol. 101, pp. 95–99, 2018, doi: 10.1016/j.compgeo.2018.04.019.
[75] Y. zhi Zhang, Y. qian Dong, J. zhou Wang, M. Wang, Y. han Cui, and X. kang Kou, 'Effects of freeze–thaw cycles on the deformation and microstructure of silt', *Cold Reg. Sci. Technol.*, vol. 239, 2025, doi: 10.1016/j.coldregions.2025.104605.
[76] Z. Fu, Q. Wu, W. Zhang, H. He, and L. Wang, 'Water Migration and Segregated Ice Formation in Frozen Ground: Current Advances and Future Perspectives', *Front. Earth Sci.*, vol. 10, 2022, doi: 10.3389/feart.2022.826961.
[77] H. Bing, P. He, C. Yang, Y. Shi, S. Zhao, and X. Bian, 'Impact of sodium sulfate on soil frost heaving in an open system', *Appl. Clay Sci.*, vol. 35, no. 3–4, pp. 189–193, 2007, doi: 10.1016/j.clay.2006.09.007.
[78] Y. Wu, S. Nakagawa, T. J. Kneafsey, B. Dafflon, and S. Hubbard, 'Electrical and seismic response of saline permafrost soil during freeze - Thaw transition', *J. Appl. Geophys.*, vol. 146, pp. 16–26, 2017, doi: 10.1016/j.jappgeo.2017.08.008.
[79] Y. Tian, Y. Lai, Z. Qin, and W. Pei, 'Numerical investigation on the thermal control performance and freeze-thaw resistance of a composite concrete pier with microencapsulated phase change materials', *Sol. Energy*, vol. 231, pp. 970–984, 2022, doi: 10.1016/j.solener.2021.12.042.
[80] K. Watanabe and T. Wake, 'Measurement of unfrozen water content and relative permittivity of frozen unsaturated soil using NMR and TDR', *Cold Reg. Sci. Technol.*, vol. 59, no. 1, pp. 34–41, 2009, doi: 10.1016/j.coldregions.2009.05.011.
[81] Z. Wen *et al.*, 'Experimental study on unfrozen water content and soil matric potential of Qinghai-Tibetan silty clay', *Environ. Earth Sci.*, vol. 66, no. 5, pp. 1467–1476, 2012, doi: 10.1007/s12665-011-1386-0.
[82] M. Elsayed *et al.*, 'A review on the applications of nuclear magnetic resonance (NMR) in the oil and gas industry: laboratory and field-scale measurements', *J. Pet. Explor. Prod. Technol.*, vol. 12, no. 10, pp. 2747–2784, 2022, doi: 10.1007/s13202-022-01476-3.
[83] Z. Y. Zhang and C. Z. Cui, 'A Review of Pore Structure Characteristics Based on Nuclear Magnetic Resonance (NMR) T2 Cutoff', *Springer Ser. Geomech. Geoengin.*, pp. 281–300, 2025, doi: 10.1007/978-981-96-2363-1_20.
[84] R. Solatpour, J. L. Bryan, and A. Kantzas, 'On estimating irreducible water saturation in tight formations using nuclear magnetic resonance relaxometry', *Soc. Pet. Eng. - SPE Canada Unconv. Resour. Conf. URC 2018*, vol. 2018-March, 2018, doi: 10.2118/189803-ms.
[85] Y. Chen, Z. Zhou, J. Wang, Y. Zhao, and Z. Dou, 'Quantification and division of unfrozen water content during the freezing process and the influence of soil properties by low-field nuclear magnetic resonance', *J. Hydrol.*, vol. 602, 2021, doi: 10.1016/j.jhydrol.2021.126719.
[86] Y. Zou, H. Jiang, E. Wang, X. Liu, and S. Du, 'Variation and prediction of unfrozen water content in different soils at extremely low temperature conditions', *J. Hydrol.*, vol. 624, 2023, doi: 10.1016/j.jhydrol.2023.129900.
[87] W. E. Kenyon, 'Nuclear magnetic resonance as a petrophysical measurement', *Nucl. Geophys.*, vol. 6, no. 2, pp. 153–171, 1992.
[88] G. Coates, L. Xiao, and M. Prammer, 'NMR logging: principles and applications', in *Haliburton Energy Services*, 1999, p. 234. [Online]. Available: http://doi.wiley.com/10.1002/cmr.1029
[89] A. Pajzderska, M. A. Gonzalez, J. Mielcarek, and J. Wąsicki, 'Water behavior in MCM-41 as a function of pore filling and temperature studied by NMR and molecular dynamics simulations', *J. Phys. Chem. C*, vol. 118, no. 41, pp. 23701–23710, 2014, doi: 10.1021/jp505490c.
[90] T. Kozlowski and E. Nartowska, 'Unfrozen Water Content in Representative Bentonites of Different Origin Subjected to Cyclic Freezing and Thawing', *Vadose Zo. J.*, vol. 12, no. 1, pp. 1–11, 2013, doi: 10.2136/vzj2012.0057.
[91] S. Feng, H. Zhang, J. Lv, M. Dyck, Q. Wu, and H. He, 'A scientometric review of research status on unfrozen soil water', *Water (Switzerland)*, vol. 13, no. 5, 2021, doi: 10.3390/w13050708.
[92] J. Bi *et al.*, 'Investigation on unfrozen water content models of freezing soils', *Front. Earth Sci.*, vol. 10, 2023, doi: 10.3389/feart.2022.1039330.
[93] Z. Xiao, L. Zhu, and Z. Hou, 'The change mechanism and a prediction model of unfrozen water content in sodium chloride soil', *Geoderma*, vol. 419, 2022, doi: 10.1016/j.geoderma.2022.115881.
[94] P. J. Williams, 'Unfrozen water content of frozen soils and soil moisture suction', *Geotechnique*, vol. 14, no. 3, pp. 231–246, 1964, doi: 10.1680/geot.1964.14.3.231.
[95] G. Cai, Y. Liu, A. Zhou, J. Li, R. Yang, and C. Zhao, 'Temperature-dependent water retention curve model for both adsorption and capillarity', *Acta Geotech.*, vol. 17, no. 11, pp. 5157–5186, 2022, doi: 10.1007/s11440-022-01657-8.
[96] K. Watanabe and Y. Osada, 'Comparison of Hydraulic Conductivity in Frozen Saturated and Unfrozen Unsaturated Soils', *Vadose Zo. J.*, vol. 15, no. 5, pp. 1–7, 2016, doi: 10.2136/vzj2015.11.0154.
[97] K. Watanabe, T. Kito, T. Wake, and M. Sakai, 'Freezing experiments on unsaturated sand, loam and silt loam', *Ann. Glaciol.*, vol. 52, no. 58, pp. 37–43, 2011, doi: 10.3189/172756411797252220.
[98] T. Ma, C. Wei, X. Xia, J. Zhou, and P. Chen, 'Soil Freezing and Soil Water Retention Characteristics: Connection and Solute Effects', *J. Perform. Constr. Facil.*, vol. 31, no. 1, 2017, doi: 10.1061/(asce)cf.1943-5509.0000851.
[99] P. B. Black and A. R. Tice, 'Comparison of soil freezing curve and soil water curve data for Windsor sandy loam', *Water Resour. Res.*, vol. 25, no. 10, pp. 2205–2210, 1989, doi: 10.1029/WR025i010p02205.
[100] K. Dunn, D. Bergman, and G. LaTorraca, *Nuclear magnetic resonance: Petrophysical and logging applications*. 2002. [Online]. Available:
http://medcontent.metapress.com/index/A65RM03P4874243N.pdf%5Cnhttp://books.google.com/books?hl=en&lr=&id=7OmAcL2qi-0C&oi=fnd&pg=PP2&dq=Nuclear+Magnetic+Resonance+Petrophysical+and+Logging+Applications&ots=EpJ5kykmiT&sig=IzgNcqy8r3FDcO4KmxgOt7jGKlM%5Cnhttp
[101] C. D. Adenutsi, Z. Li, Z. Xu, and L. Sun, 'Influence of net confining stress on NMR T2 distribution and two-phase relative permeability', *J. Pet. Sci. Eng.*, vol. 178, pp. 766–777, 2019, doi: 10.1016/j.petrol.2019.03.083.

[102] V. Gautam *et al.*, 'Harnessing NMR technology for enhancing field crop improvement: applications, challenges, and future perspectives', *Metabolomics*, vol. 21, no. 2, 2025, doi: 10.1007/s11306-025-02229-z.
[103] W. Skierucha, *Time Domain Reflectometry: Temperature-dependent Measurements of Soil Dielectric Permittivity*. 2011. doi: 10.5772/17162.
[104] G. Kargas and K. X. Soulis, 'Performance evaluation of a recently developed soil water content, dielectric permittivity, and bulk electrical conductivity electromagnetic sensor', *Agric. Water Manag.*, vol. 213, pp. 568–579, 2019, doi: 10.1016/j.agwat.2018.11.002.
[105] M. I. Abdulraheem *et al.*, 'Recent Advances in Dielectric Properties-Based Soil Water Content Measurements', *Remote Sens.*, vol. 16, no. 8, 2024, doi: 10.3390/rs16081328.
[106] X. Zhou, J. Zhou, W. Kinzelbach, and F. Stauffer, 'Simultaneous measurement of unfrozen water content and ice content in frozen soil using gamma ray attenuation and TDR', *Water Resour. Res.*, vol. 50, no. 12, pp. 9630–9655, 2014, doi: 10.1002/2014WR015640.
[107] B. Caicedo, 'Physical modelling of freezing and thawing of unsaturated soils', *Geotechnique*, vol. 67, no. 2, pp. 106–126, 2017, doi: 10.1680/jgeot.15.P.098.
[108] G. N. Flerchinger, M. S. Seyfried, and S. P. Hardegree, 'Using Soil Freezing Characteristics to Model Multi-Season Soil Water Dynamics', *Vadose Zo. J.*, vol. 5, no. 4, pp. 1143–1153, 2006, doi: 10.2136/vzj2006.0025.
[109] T. F. Azmatch, D. C. Sego, L. U. Arenson, and K. W. Biggar, 'Using soil freezing characteristic curve to estimate the hydraulic conductivity function of partially frozen soils', *Cold Reg. Sci. Technol.*, vol. 83–84, pp. 103–109, 2012, doi: 10.1016/j.coldregions.2012.07.002.
[110] E. J. A. Spaans and J. M. Baker, 'The Soil Freezing Characteristic: Its Measurement and Similarity to the Soil Moisture Characteristic', *Soil Sci. Soc. Am. J.*, vol. 60, no. 1, pp. 13–19, 1996, doi: 10.2136/sssaj1996.03615995006000010005x.
[111] G. P. Newman and G. W. Wilson, 'Heat and mass transfer in unsaturated soils during freezing', *Can. Geotech. J.*, vol. 34, no. 1, pp. 63–70, 1997, doi: 10.1139/cgj-34-1-63.
[112] Z. Liu, B. Zhang, X. Yu, and J. Tao, 'A new method for soil water characteristic curve measurement based on similarities between soil freezing and drying', *Geotech. Test. J.*, vol. 35, no. 1, 2012, doi: 10.1520/GTJ103653.
[113] R. W. R. Koopmans and R. D. Miller, 'Soil Freezing and Soil Water Characteristic Curves', *Soil Sci. Soc. Am. J.*, vol. 30, no. 6, pp. 680–685, 1966, doi: 10.2136/sssaj1966.03615995003000060011x.
[114] L. J. West, K. Handley, Y. Huang, and M. Pokar, 'Radar frequency dielectric dispersion in sandstone: Implications for determination of moisture and clay content', *Water Resour. Res.*, vol. 39, no. 2, 2003, doi: 10.1029/2001WR000923.
[115] J. D. G. Teruel, 'Modeling of soil dielectric properties. Application in sensor design for precision agriculture control systems', 2022, [Online]. Available: https://repositorio.upct.es/handle/10317/11899%0Ahttps://repositorio.upct.es/bitstream/handle/10317/11899/jdgt.pdf?sequence=1&isAllowed=y
[116] M. Zhang, X. Zhang, Y. Lai, J. Lu, and C. Wang, 'Variations of the temperatures and volumetric unfrozen water contents of fine-grained soils during a freezing–thawing process', *Acta Geotech.*, vol. 15, no. 3, pp. 595–601, 2020, doi: 10.1007/s11440-018-0720-z.
[117] J. Lu, W. Pei, X. Zhang, J. Bi, and T. Zhao, 'Evaluation of calculation models for the unfrozen water content of freezing soils', *J. Hydrol.*, vol. 575, pp. 976–985, 2019, doi: 10.1016/j.jhydrol.2019.05.031.
[118] S. Zhang *et al.*, 'Unraveling the molecular freezing behavior of water on a calcium silicate hydrate matrix', *Phys. Chem. Chem. Phys.*, vol. 26, no. 6, pp. 5115–5127, 2024, doi: 10.1039/d3cp05213c.
[119] M. Fleury, T. Gimmi, and M. Mazurek, 'Porewater Content, Pore Structure and Water Mobility in Clays and Shales from NMR Methods', *Clays Clay Miner.*, vol. 70, no. 3, pp. 417–437, 2022, doi: 10.1007/s42860-022-00195-4.
[120] P. Eizaguirre *et al.*, 'Exploring two regimes of water mobility in unsaturated expansive clay using NMR relaxometry', *Appl. Clay Sci.*, vol. 251, 2024, doi: 10.1016/j.clay.2024.107324.
[121] M. Zhang, W. Pei, S. Li, J. Lu, and L. Jin, 'Experimental and numerical analyses of the thermo-mechanical stability of an embankment with shady and sunny slopes in permafrost regions', *Appl. Therm. Eng.*, vol. 127, pp. 1478–1487, 2017, doi: 10.1016/j.applthermaleng.2017.08.074.
[122] V. Genuchten, 'A closed-form equation for predicting the hydraulic conductivity of unsaturated soils', *Soil Sci. Soc. Am. J.*, vol. 44, pp. 892\textrm{-}897, 1980.
[123] S. F. Santoyo and T. Baser, 'A Review of the Existing Data on Soil-Freezing Experiments and Assessment of Soil-Freezing Curves Derived from Soil–Water Retention Curves', *J. Cold Reg. Eng.*, vol. 36, no. 1, 2022, doi: 10.1061/(asce)cr.1943-5495.0000271.
[124] Olivier Coussy, 'Poromechanics of freezing materials', *J. Mech. Phys. Solids*, vol. 53, no. 8, pp. 1689–1718, 2005.
[125] A. G. Steven and S. S. Ronald, 'Calculating capillary pressures in frozen and ice-free soils below the melting temperature', *Environ. Geol.*, vol. 42, pp. 130–136, 2002.
[126] M. Bittelli, M. Flury, and G. S. Campbell, 'A thermodielectric analyzer to measure the freezing and moisture characteristic of porous media', *Water Resour. Res.*, vol. 39, no. 2, 2003, doi: 10.1029/2001WR000930.
[127] S. Nishimura, A. Gens, S. Olivella, and R. J. Jardine, 'Thm-coupled finite element analysis of frozen soil: Formulation and application', *Geotechnique*, vol. 59, no. 3, pp. 159–171, 2009, doi: 10.1680/geot.2009.59.3.159.
[128] M. Vitel, A. Rouabhi, M. Tijani, and F. Guérin, 'Modeling heat and mass transfer during ground freezing subjected to high seepage velocities', *Comput. Geotech.*, vol. 73, pp. 1–15, 2016, doi: 10.1016/j.compgeo.2015.11.014.
[129] J. Zhou, 'Experimental study on characteristics of unfrozen water in clay mineral and its effect on sand thawing characteristics', Xuzhou: China University of Mining and Technology., 2020.
[130] H. Wen, J. Bi, and D. Guo, 'Evaluation of the calculated unfrozen water contents determined by different measured subzero temperature ranges', *Cold Reg. Sci. Technol.*, vol. 170, 2020, doi: 10.1016/j.coldregions.2019.102927.
[131] W. Skierucha, *Time Domain Reflectometry: Temperature-dependent Measurements of Soil Dielectric Permittivity*. 2011. doi: 10.5772/17162.
[132] C. Wang, K. Li, Q. Chen, J. Ren, X. jia He, and S. Li, 'Revealing the freezing-thawing hysteretic mechanisms of soil–water system based on soil microstructure', *Geoderma*, vol. 449, 2024, doi: 10.1016/j.geoderma.2024.116986.
[133] C. Wang, Y. Lai, F. Yu, and S. Li, 'Estimating the freezing-thawing hysteresis of chloride saline soils based on the phase transition theory', *Appl. Therm. Eng.*, vol. 135, pp. 22–33, 2018, doi: 10.1016/j.applthermaleng.2018.02.039.
[134] J. Lu, M. Zhang, X. Zhang, and Z. Yan, 'Experimental study on the unfrozen water content and the freezing temperature during freezing and thawing processes', *Yanshilixue Yu Gongcheng Xuebao/Chinese J. Rock Mech. Eng.*, vol. 36, no. 7, pp. 1803–1812, 2017, doi: 10.13722/j.cnki.jrme.2016.1433.
[135] W. Huang, Q. B. Liu, W. Xiang, L. Z. Lang, D. S. Cui, and J. E. Wang, 'Hydration mechanism and microscopic water retention model of clay at high suction range', *Yantu Gongcheng Xuebao/Chinese J. Geotech. Eng.*, vol. 40, no. 7, pp. 1268–1276, 2018, doi: 10.11779/CJGE201807013.
[136] C. Wang *et al.*, 'Predicting the Soil Freezing Characteristic From the Particle Size Distribution Based on Micro-Pore Space

Geometry', *Water Resour. Res.*, vol. 58, no. 1, 2022, doi: 10.1029/2021WR030782.
[137] G. P. Brovka and S. N. Ivanov, 'Calculation of temperature fields in the ground with water-ice phase transitions in the temperature spectrum', *J. Eng. Phys. Thermophys.*, vol. 77, no. 6, pp. 1192–1200, 2004, doi: 10.1007/s10891-005-0014-9.
[138] X. Z. Xu, J. C. Wang, and L. X. Zhang, 'Frozen soil physics', *Sci. Press*, pp. 60–68, 2010.
[139] C. Wang, 'Study of hydro-thermal characteristics and hysteretic mechanisms of soils under freezing and thawing processes', Lanzhou University, 2018. [Online]. Available: https://scholar.google.com/scholar_lookup?title=Study of hydro-thermal characteristics and hysteretic mechanisms of soils under freezing and thawing processes&publication_year=2018&author=C. Wang
[140] K. Watanabe, M. Takeuchi, Y. Osada, and K. Ibata, 'Micro-Chilled-Mirror Hygrometer for Measuring Water Potential in Relatively Dry and Partially Frozen Soils', *Soil Sci. Soc. Am. J.*, vol. 76, no. 6, pp. 1938–1945, 2012, doi: 10.2136/sssaj2012.0070.